Computers and Fluids 269 (2024) 106121

Contents lists available at ScienceDirect

Computers and Fluids

journal homepage: www.elsevier.com/locate/compfluid

Heat flux predictions for hypersonic flows with an overset near body solver on an adaptive block-structured Cartesian off-body grid

Joel A. McQuaid, Christoph Brehm [*]

Department of Aerospace Engineering, University of Maryland, College Park, MD 20740, USA

ARTICLE INFO

Keywords:
Cartesian grid solver
Hypersonic flows
Thermochemical non-equilibrium
Near body solver
Strand grid
Heat flux predictions

ABSTRACT

The manual volume mesh generation process for body-fitted CFD codes can be a time-intensive process, particularly for complex flight vehicles. The work shown here presents a hybrid body-fitted/Cartesian overset CFD solver capable of automatic volume mesh generation capabilities and accurate surface heating predictions. The solver uses a body-conformal near body solver for capturing boundary layer effects and an off-body Cartesian solver with adaptive mesh refinement for shock and wake tracking within the CHAMPS CFD code. The formulated near body Cartesian solver is the first of its kind to be applied within the context of low and high enthalpy, hypersonic viscous flows. The developed solver is validated on a Mach 9.47 Mars Science Lander and a Mach 6 Orion Crew Exploration Vehicle in a low-enthalpy flow at various non-zero angles of attack followed by a Mach 25.2 AS-202 capsule at a 17.8-degree angle of attack for Earth re-entry. Validation is shown based on grid convergence studies as well as good agreement to available numerical and experimental data in consideration of surface heating and surface pressure predictions.

1. Introduction

Heating loads during re-entry and ballistic environments can be extreme, causing significant thermo-chemical ablation on the thermal protection shield (TPS) and high-temperature effects to occur in the post-shock region. Simulating the coupled interaction between the high-enthalpy flow-field and the TPS requires a robust coupling infrastructure and accurate numerical methods for capturing the boundary layer profiles in a hypersonic viscous flow. Important considerations need to be made regarding mesh alignment with the shock front, grid quality, low-dissipation numerical schemes, correct modeling of high-temperature effects, and efficient mesh motion algorithms when designing a fluid solver for simulating ablative environments.

As far as the authors are aware, all currently available fluid ablation interaction (FAI) solvers employ manually generated body-fitted, volume grids for the entire fluid domain to accurately capture surface heating loads efficiently. Body-fitted codes allow for the use of high aspect ratio stretched grids in the vicinity of the surface which becomes particularly effective when seeking to reduce the total number of grid points required for a given geometry. However, even for simple geometries, mesh generation that employs both shock alignment and wall orthogonality may prove challenging while also ensuring high grid quality. For 3D geometries, this process can be an exceptionally time-consuming manual process. In consideration of FAI solvers, thought must also be given to mesh motion algorithms as the TPS ablates. The additional requirement of maintaining a high quality grid, shock alignment, and wall orthogonality after undergoing significant levels of surface recession is critical to ensuring heating loads are still accurately captured after significant surface topology changes have occurred.

Automatic meshing capabilities are essential to avoid much of the previously mentioned challenges. This need for a more automated case setup and simulation process has been expressed as part of the CFD Vision 2030 [1]. Cartesian grid and Immersed Boundary (IB) solvers are readily available to meet this task for automatic meshing functionality, however, Cartesian grids severely under perform in regards to overall computational cost for hypersonic viscous flow applications. The need to resolve the strong near-wall gradients for viscous flows requires cell Reynolds numbers on the order of unity at the surface. With the lack of body alignment from the Cartesian grid, near-wall cell aspect ratios are generally restricted to around 1 resulting in the need for millions or tens of millions of cells for even the most simple 2D/3D geometries [2].

To date, Cartesian grids have seen limited applications to high-speed viscous flows, and when used for such applications, they require prohibitively more computational resources versus more traditional body-fitted approaches. Some past work include Brahmachary et al. [3], Sekhar et al. [4], and Arslanbekov et al. [5] which both employed Cartesian grids to capture heating loads for various geometries, however, these cases were generally limited to either non-blunt geometries

---

[*] Corresponding author.
E-mail address: cbrehm1@umd.edu (C. Brehm).

https://doi.org/10.1016/j.compfluid.2023.106121
Received 17 June 2023; Received in revised form 6 October 2023; Accepted 13 November 2023

and/or low Reynolds numbers which resulted in thicker boundary layers than generally seen on hypersonic vehicles. In the work of Baskaya et al. [6], two immersed boundary method (IBM) solvers are employed to simulating high-speed viscous flows and for a 2D ablator test case. The INCA solver employs a finite-volume IBM solver with a cut-cell framework at the surface to ensure a fully conservative methodology while the CHESS solver employs a finite-volume scheme with a ghost-cell convective scheme which is known to be a non-conservative approach. Significant heat flux under-predictions are shown for the CHESS solver versus both INCA and US3D as seen by other Cartesian grid solvers for similar high-speed, blunt body geometries. The work demonstrates that a conservative convective and viscous scheme is essential to correctly capturing heating loads, however, the drawback of low aspect ratio cells at the surface continues to raise significant concerns on the viability of Cartesian grids for viscous applications.

The work presented here seeks to extend the current application of Cartesian grid solvers to high-enthalpy viscous flows via a hybrid Cartesian/body-fitted solver. The formulated solver employs a near body solver (NBS) which automatically generates a body-conformal grid for capturing near-wall gradients efficiently and coupling this solution with an off-body Cartesian solver for simulating high-speed flight regimes. The so-called CHAMPS NBS-Cart (short for NBS-Cartesian) solver introduced in this work has demonstrated high levels of accuracy in heat flux predictions for high-enthalpy environments as well as a robust infrastructure for coupling into the Kentucky Aerothermodynamics and Thermal Protection System (KATS) material response solver for simulating TPS thermal response, surface recession, and surface thermo-chemistry while simultaneously under-going topology changes. All aspects of the volume mesh generation process for both solvers is fully automatic, requiring only a surface mesh, and with the use of adaptive mesh refinement (AMR), the shock, surface topology changes, and wake structure are also automatically tracked. The implemented NBS-Cart solver in CHAMPS provides order of magnitude savings in computational costs versus a fully-resolved Cartesian/IB solver approach and approaches a more comparable computational cost to a body-fitted solution in terms of the total number of grid points.

The use of an NBS or strand grid solver for assisting Cartesian grid solvers in simulating high-speed viscous flows is a relatively new and emerging technology being developed by some research teams. In the work of Meakin et al. [2], the NBS NSU3D is coupled to the block-structured Cartesian solver SAMARC to simulate the vortex-shedding of a sphere at a Reynolds number of 300. The NBS is able to correctly capture the separation point on the cylinder and the AMR is used to track the turbulent wake structure. Strand grid solvers have also been employed to simulate isolated rotors in hover by Wissink et al. [7] and was compared back against fully unstructured and mixed unstructured-Cartesian methods. The strand-Cartesian solver with AMR showed superior performance in preserving the vortex core coming off the rotor tip versus the other two methods which may be due to better quality grid in the boundary layer due to the strand grid solver and the ability to easily implement higher order schemes in the off-body regions due to the use of Cartesian grids. In terms of computational cost, for increasingly large problems, strand grid/NBS solvers compose only a small fraction of the total computational cost for a given problem, especially for cases where significant off-body resolution is required for resolving shock structures or wake features [8]. Significant work in the implementation of coupled NBS codes is also being done as part of the CREATE-AV program such as the coupling of the NASA FUN3D code as the unstructured NBS to the SAMARC Cartesian solver [9] as well as the KCFD/SAMAir solver which uses the KCFD solver in Kestrel as the NBS and the SAMAir Cartesian solver [10] as the off-body solver to name a few. Both solvers also use an overset coupling approach between the NBS and Cartesian solvers, although the functionality of the interpolation differs from the approach used in this work. The validation work from these coupled solvers primarily targeted rotor and/or rotor-fuselage configurations. None of these prior works, however, were tested within the supersonic or hypersonic flow environments, leading to the primary motivation for this work; to provide a more automated CFD solver capable of accurate heating predictions under extreme re-entry conditions. The NBS-Cart solver shown in this work seeks to extend the application of these solvers to accurate heat flux predictions and ablative flight regimes while accounting for high-temperature effects and multi-component fluid models.

The CHAMPS NBS solver used here has been employed in the past for various coupling frameworks. The NBS solver coupling to the CHAMPS IBM solver via a wall-model formulation was demonstrated and validated for various perfect gas and high enthalpy flows in Ref. [11]. The NBS provided surface viscous fluxes to the IBM solver at grid line intersection points on the surface for closure of the viscous scheme while employing a ghost-point convective scheme for the convective fluxes. The NBS was then switched to an overset coupling approach (NBS-Cart solver) to enhance robustness for moving boundary problems. The NBS-Cart solver was then validated for a variety of low and high temperature ablator problems in Refs. [12–16]. The validation against Camphor (low-temperature ablator) demonstrated the high levels of accuracy that was achieved with the NBS-Cart solver while undergoing massive levels of surface topology changes. Graphite ablation was also simulated to showcase the high-enthalpy capabilities of the NBS-Cart solver while also capturing surface production due to thermo-chemical ablation as well as the solver robustness while undergoing significant surface heating. The prior works show that the current coupling of the NBS-Cart solver to KATS is efficient and able to accurately capture surface recession time histories.

The objective of this work is to extend the NBS-Cart solver into three-dimensional applications and validate the methodology for low and high-enthalpy flows seen in real-world re-entry problems. The extension of the CHAMPS NBS into 3D requires a more generalized framework for grid generation and numerical flux calculations due to the unstructured nature of the surface grids employed here. Wall-normal structured layouts are retained for efficient line implicit methods to allow for rapid convergence to steady-state solutions.

This work will proceed as follows. First, the governing equations surrounding a perfect gas and a fluid in thermo-chemical non-equilibrium are discussed in Section 2. Next, the CHAMPS NBS-Cart solver implementation is given in Section 3. Then, validation results of the CHAMPS NBS-Cart solver for various low and high-enthalpy test cases is shown with comparison against experimental and numerical sources in Section 4.

2. Governing equations

In this work, both perfect gas and multi-component fluid models are employed for validation of the NBS-Cart solver. The governing equations for a multi-component fluid in thermo-chemical non-equilibrium (TCNE) are shown here with the perfect gas equations being obtained by omitting the TCNE source term and assuming a single species mixture. To simulate Earth re-entry, a 5-species air model (N_2, O_2, NO, N, and O) was employed in this work. Thermal non-equilibrium is modeled using the two temperature model by Park [17] which assumes that the translational and rotational models are in equilibrium at a single temperature T while the vibrational and electronic modes are modeled separately by T_{ve}. Ionization and radiative effects within the fluid flow field are neglected in this work to reduce the computational cost of the employed gas model and so $T_{ve} = T_v$. A chemically-reacting flow in TCNE may be modeled using the compressible Navier–Stokes equations as in Eq. (1)

$$\frac{\partial \boldsymbol{U}}{\partial t} + \nabla \cdot \left(\boldsymbol{F} - \boldsymbol{F_d} \right) = \boldsymbol{W}, \tag{1}$$

where $\boldsymbol{U}$ is the conservative state vector, $\boldsymbol{P}$ is the primitive state vector, $\boldsymbol{F}$ is the convective flux, $\boldsymbol{F_d}$ is the viscous flux and $\boldsymbol{W}$ is the thermo-chemical source term. The primitive and conservative state vectors are given in Eq. (2) where ρ_s is the species density, ρ is the total fluid density, $\boldsymbol{V} = \{u, v, w\}^T$ is the fluid velocity vector with its specified components in the Cartesian reference frame, and E and E_v are the total energy and vibrational energy components per unit volume

$$\boldsymbol{U} = \begin{Bmatrix} \rho_1 \\ \vdots \\ \rho_{ns} \\ \rho u \\ \rho v \\ \rho w \\ E \\ E_v \end{Bmatrix} \text{ and } \boldsymbol{P} = \begin{Bmatrix} \rho_1 \\ \vdots \\ \rho_{ns} \\ u \\ v \\ w \\ T \\ T_v \end{Bmatrix}. \tag{2}$$

Eq. (3) gives the convective and viscous flux vectors such that $\hat{u}$ is defined as the contravariant velocity, p is the mixture pressure, $\boldsymbol{J}_s$ is the mass diffusion flux vector of species s, $\boldsymbol{\tau}$ is the viscous stress tensor, $\boldsymbol{q_{tr}}$ and $\boldsymbol{q_{ve}}$ are the heat flux components for the translational/rotational and vibrational energy modes respectively, and h_s is the enthalpy of species s.

$$\boldsymbol{F} = \begin{Bmatrix} \rho_1 \hat{u} \\ \vdots \\ \rho_{ns} \hat{u} \\ \rho u \hat{u} + p\delta_{1i} \\ \rho v \hat{u} + p\delta_{2i} \\ \rho w \hat{u} + p\delta_{3i} \\ (E+p)\hat{u} \\ E_v \hat{u} \end{Bmatrix} \text{and } \boldsymbol{F_d} = \begin{Bmatrix} -\boldsymbol{J_1} \\ \vdots \\ -\boldsymbol{J_{ns}} \\ \boldsymbol{\tau_{1i}} \\ \boldsymbol{\tau_{2i}} \\ \boldsymbol{\tau_{3i}} \\ \boldsymbol{q_{tr}} + \boldsymbol{q_{ve}} - \sum_{s=1}^{ns} \boldsymbol{J}_s h_s + \boldsymbol{\tau} \cdot \boldsymbol{V} \\ \boldsymbol{q_v} - \sum_{s=1}^{ns} \boldsymbol{J}_s e_{v,s} \end{Bmatrix}. \tag{3}$$

For a perfect gas assumption, a Prandtl number of 0.72 is assumed with the viscosity being computed using Sutherlands law. Mixture transport properties for 5-species air is computed using the Gupta mixing rule [18]. Further details on the TCNE transport property modeling can be found in Appendix B.

2.1. Source terms

The thermo-chemical non-equilibrium source term used in this work is given as

$$\boldsymbol{W} = \left\{ \omega_1 \quad \cdots \quad \omega_{ns} \quad 0 \quad 0 \quad 0 \quad 0 \quad S_{t2v} + S_{c2v} \right\}^T, \tag{4}$$

where ω_s is the net chemical production rate of species s, S_{t2v} is the translational to vibrational energy exchange, and S_{c2v} is the chemical to vibrational energy exchange. The chemical source term used in this work contains 5 reactions; 3 dissociation reactions and 2 exchange reactions. The complete list of reactions being modeled is

1. $N_2 + M \rightleftharpoons N + N + M$
2. $O_2 + M \rightleftharpoons O + O + M$
3. $NO + M \rightleftharpoons N + O + M$
4. $O_2 + N \rightleftharpoons NO + O$
5. $N_2 + O \rightleftharpoons NO + N$

For the chemical source term, $\dot{w}_{sr}$ is the chemical production rate of species s in reaction r and is given by

$$\dot{w}_{sr} = (\nu''_{sr} - \nu'_{sr}) \left[k_{fr} \prod_{j=1}^{ns} \left(\frac{\rho_j}{M_j} \right)^{\nu'_{jr}} - k_{br} \prod_{j=1}^{ns} \left(\frac{\rho_j}{M_j} \right)^{\nu''_{jr}} \right], \tag{5}$$

and the source term, ω_s, by

$$\omega_s = M_s \sum_{r=1}^{nr} \dot{w}_{sr}, \tag{6}$$

where, for a given reaction r, ν' is the stoichiometric coefficient for the reactants, ν'' is the stoichiometric coefficient for the products, k_{fr} is the forward reaction rate, k_{br} is the backward reaction rate, and nr is the number of reactions. Further details on the equations used to compute the forward and backward rates as well as the reaction rates used in this work has been provided in Appendices A–C, respectively.

2.2. Surface boundary conditions

To simulate the AS-202 capsule and compare against the results of the DPLR solver [19], a diffusion-limited fully catalytic surface must be included into the NBS structure with a radiative equilibrium temperature boundary condition. The energy balance at the surface may be written as

$$q_{rad} = q_{tr} + q_v + q_{diff}, \tag{7}$$

where q_{rad} is the radiative heat flux back to the freestream, q_{tr} is the translational/rotational heat flux, q_v is the vibrational energy heat flux and q_{diff} is the enthalpy diffusion flux. Expanding the terms yields

$$\epsilon\sigma \left(T_w^4 - T_{ref}^4 \right) = \kappa_{tr} \left(\frac{T - T_w}{\Delta\eta} \right) + \kappa_v \left(\frac{T_v - T_w}{\Delta\eta} \right) + \sum_{s=1}^{ns} \rho D_s h_s \frac{Y_s - Y_{s,w}}{\Delta\eta}, \tag{8}$$

where ϵ is the surface emissivity, σ is the Stefan–Boltzmann constant, T_{ref} is the reference temperature which is set equal to the freestream temperature, and $\Delta\eta$ is the distance from the wall surface centroid to the first element centroid off the wall where the temperature and mass fractions are taken to compute the necessary wall-normal gradients. The two temperatures are assumed to equilibrate at the wall and all transport properties are computed based on the wall state. The solution to Eq. (8) is found via Newton solve given as

$$T_w^{k+1} = T_w^k - \frac{f(T_w^k)}{f'(T_w^k)}, \tag{9}$$

where

$$f(T_w) = \kappa_{tr} \left(\frac{T - T_w}{\Delta\eta} \right) + \kappa_v \left(\frac{T_v - T_w}{\Delta\eta} \right) + \sum_{s=1}^{ns} \rho D_s h_s \frac{Y_s - Y_{s,w}}{\Delta\eta} - \epsilon\sigma \left(T_w^4 - T_{ref}^4 \right) \tag{10}$$

and

$$f'(T_w) \approx -\frac{\kappa_{tr}}{\Delta\eta} - \frac{\kappa_v}{\Delta\eta} - 4\epsilon\sigma T_w^3, \tag{11}$$

such that the transport properties are assumed constant in the near-wall region to simplify the derivative computation. The solver is iterated on index, k, until a residual of 1×10^{-12} is reached. The fully catalytic wall in this work models a diffusion-limited recombination of atomic nitrogen and oxygen at the surface. From Park [20], the recombination rates for atomic species may be given as

$$\dot{\omega}_{N,w} = -\gamma_N \rho_{N,w} \sqrt{\frac{R_N T_w}{2\pi}} \tag{12}$$

and

$$\dot{\omega}_{O,w} = -\gamma_O \rho_{O,w} \sqrt{\frac{R_O T_w}{2\pi}}. \tag{13}$$

The above equations give the recombination rates of atomic nitrogen and oxygen based on the species gas constant R_s, wall temperature T_w, species density at the wall $\rho_{s,w}$, and catalytic efficiency γ_s which is set to 1 for the AS-202 test case. Based on the molecular dissociation reactions for 5-species air, the atomic recombination rates must exactly balance the molecular recombination rate. Then, from the surface mass balance equation

$$\rho_w D_s \frac{Y_s - Y_{s,w}}{\Delta\eta} = \dot{\omega}_s, \tag{14}$$

it is shown that the species diffusion flux to the wall must balance the recombination rate at the surface. From these equations, a system of ns by ns equations can be solved for the new wall mass fractions. Within each Newton iteration of the radiative equilibrium solver, the wall mass fractions are recomputed to ensure the two boundary conditions mutually converge on the correct state at each instant in time.

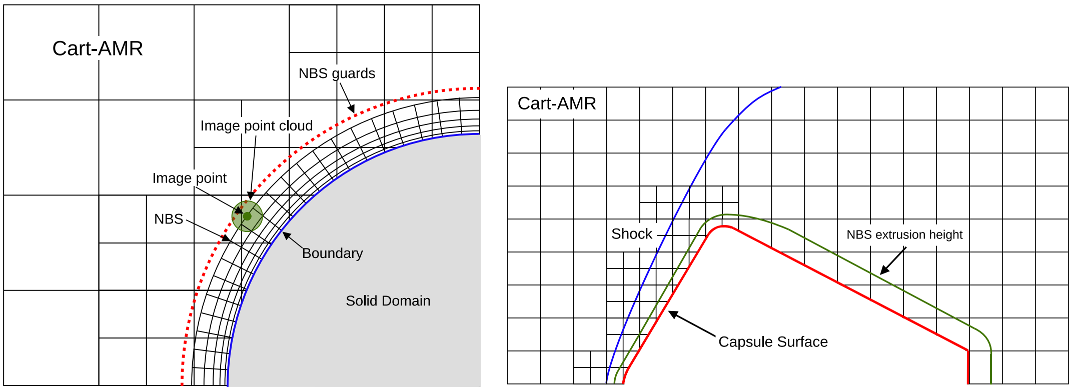

Fig. 1. NBS-Cart solver overview for a 2D cylinder test case (left) and a hypersonic capsule test case (right) with a detached shock front.

3. CHAMPS NBS-Cart solver

A brief overview of the CHAMPS NBS-Cart solver algorithm is provided here before outlining specific details regarding the formulation of the NBS including the mesh generation process, governing equations, and numerical treatment as well as the coupling of the NBS solution with the off-body Cartesian grid. The numerical treatment employed in this work for the Cartesian solver is also briefly described for shock-capturing on non-aligned grids at high Mach numbers.

3.1. NBS-Cart overview

The NBS-Cart solver employs a overset mesh topology to leverage the algorithmic efficiencies related to both Cartesian grid and body-fitted grid solvers. The CHAMPS Cartesian grid solver is capable of automatic mesh generation via adaptive mesh refinement (AMR) such that a surface mesh is provided to CHAMPS and a block-structured Cartesian grid is generated around it based on user-supplied settings at the initialization phase. The Cartesian grid is then adaptively changed during run time for shock and wake tracking as required to ensure adequate grid resolution in regions of importance (see Section 3.7 for more details). The Cartesian grid will be under resolved within the boundary layer region and, hence, a NBS is employed in this area. The NBS automatically extrudes out a volume grid based on the provided surface mesh to the Cartesian solver which is used to resolve the near-wall gradients. At the surface, the NBS employs a traditional wall boundary condition (no-slip, isothermal wall for example) while at the tip of each ray, denoted as the NBS overset interface, the NBS is coupled into the Cartesian solver solution. Image points are placed at the tip of each ray emanating from the surface and the Cartesian solution is sampled onto each image point. This image point state is held fixed and used in combination with the NBS interior flow state to extrapolate flow conditions into guard cells located on the opposite side of the NBS overset interface.

A two dimensional schematic of the NBS-Cart solver layout is shown in Fig. 1(a) for a cylinder test case. The figure shows the body-fitted NBS grid that has been extruded out from the surface with the green point at the tip of one NBS ray denoting the image point used at the overset interface. The image point and interior point states are then used to extrapolate conditions into the marked red cells which are used as guard cells at the overset interface to facilitate higher-order schemes. Fig. 1(b) shows a similar layout for a capsule geometry with the detached shock marked as the blue curve ahead of the vehicle. The Cartesian AMR is used to refine blocks in the vicinity of the shock front with the green curve representing the location of the NBS overset interface relative to the shock interface. The overset interface couples into the Cartesian solution within the shock layer for all cases in this work. A second overset interpolation is used to transfer near-wall data from the NBS to the Cartesian solver. This second overset interpolation injects updated flow state data into the first 3–4 layers of Cartesian cells located right at the geometry surface, effectively removing any need for irregular point treatments typically used by IBM solvers.

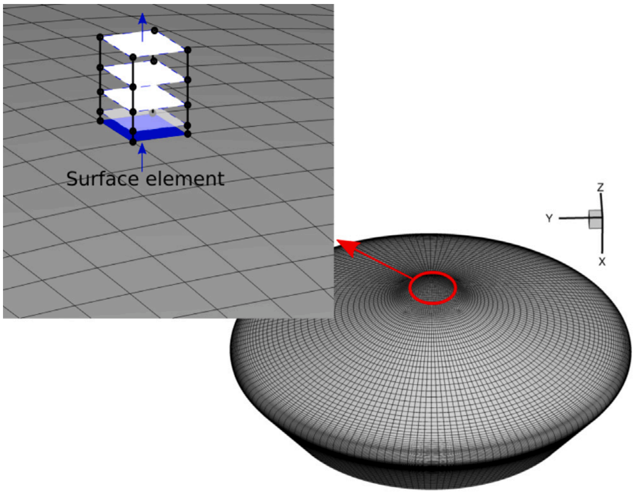

Fig. 2. NBS grid generation on a sample MSL capsule with a quadrilateral surface topology.

3.2. NBS grid generation

As part of the CHAMPS Cartesian grid solver, a surface mesh composed of any arbitrary set of polyhedrals is provided as an input at start-up. This surface mesh is used as the basis for the NBS grid generation procedure. The surface grid is first partitioned before proceeding with the grid generation. Since the NBS is solved in a sequential manner with the Cartesian grid solver, the surface grid is partitioned equally across all processors to maintain load balancing and strong scalability to large-scale models. Each processor identifies neighboring surface elements to its own partition to facilitate the MPI exchanges of various data at each iteration or during linear solver iterations. The number of identified neighboring surface elements is dependent on the order of the employed numerical scheme. Next, surface node normals are computed as a distance weighted average of all surface elements that share that surface node. Then, an identical wall-normal node distribution is applied for all surface nodes to generate the body conformal grid layout as depicted in Fig. 2.

To minimize reconstruction errors at the NBS overset and surface boundaries caused by rapid changes in cell sizes, the cell size distribution in the wall-normal direction is modified from a pure stretching

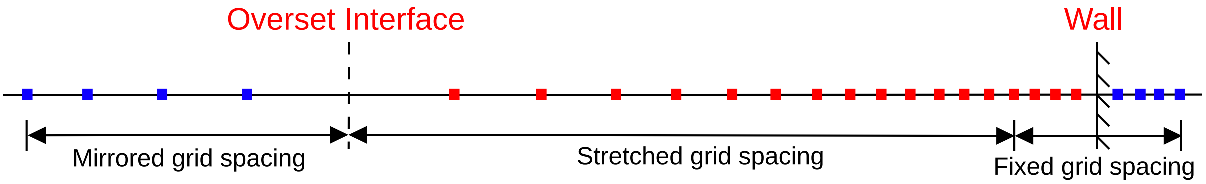

Fig. 3. NBS grid generation schematic along a 1D line segment showing mesh generation treatment near the overset interface and the surface.

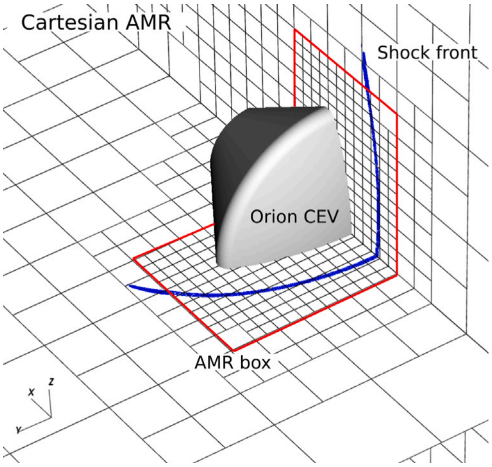

Fig. 4. Sample Cartesian grid block-structure around the Orion CEV showing variable boundary refinement to resolve the fore and aft-body. Shock front is colored via a Ducros sensor from numerical simulations shown later and the red box denotes the region in which the shock tracking AMR is active.

function. Maintaining the interior schemes formal order of accuracy at boundaries requires a sufficient number of guard cells to avoid order reduction due to a reduced stencil size. At the NBS overset interface, to remain consistent with the last several layers of cells in the interior of the grid, the cell size is mirrored over the interface such that the first guard cell centroid is equidistant from the interface as the last interior cell. Similarly, the second guard cell centroid will be equidistant from the NBS overset interface as the second last interior cell and so on. At the geometry surface, the cell size is held fixed at the user specified first cell size for as many cells as there are guard cells. A schematic of this procedure is shown in Fig. 3 for a sample 1D grid generation assuming four guard cells are specified. The grid stretching is exaggerated for clarity and all cases in this work use two guard cells for consistency with the stencil width of a third order MUSCL reconstruction on the NBS grid.

In consideration of aft body modeling, significant computational costs can be incurred by maintaining a constant boundary refinement on the Cartesian grid. Fine mesh spacing is maintained on the fore body to properly capture the shock and to ensure sufficient resolution exists between the shock front and fore body, however, the aft body sees no such restriction and can be captured well with coarser Cartesian cells. The CHAMPS solver is capable of employing variable boundary refinement AMR capabilities to provide more targeted grid resolution [21] as shown in Fig. 4. The NBS grid generation is formulated to perform variable extrusion heights based on the detected local Cartesian cell size at the surface. This methodology allows for the NBS height to scale proportionately with the Cartesian resolution to facilitate a stable coupling.

During the grid generation process, the NBS identifies the local Cartesian grid block at the base of its ray protruding from the surface and computes the minimum grid spacing in that block. Each NBS ray then independently computes its own extrusion height as a function of the identified minimum Cartesian spacing as outlined later in Section 3.6. This leads to the resulting NBS structure shown in Fig. 5(a). Discontinuities in the NBS extrusion height are expected and so a smoothing operation is performed next to gradually grow the NBS grid from regions of smaller Cartesian spacing to regions of larger Cartesian spacing as shown in Fig. 5(b). The resulting grid structure provides an ideal grid for capturing both the fore and aft body boundary layer profiles with smooth transitions in grid cell sizing. It is important to note that the extrusion height smoothing operation only modifies the growth rate of the stretched point distributions and the total extrusion height and do not modify the first cell height at the surface or degrade the wall orthogonality sought from prior steps of the grid generation process.

The smoothing process itself is a relatively simple process and is fully parallelized across all processors. Each processor identifies a subset of interior, exchange, and domain boundary surface elements from which to build its grid (can be seen in Fig. 6). Based on this subset of surface elements, an associated list of surface nodes is identified, with many nodes being claimed by several processors due to the overlapping grid structure (for MPI communications of flow-field data). The local NBS extrusion height is a data quantity stored at every surface node. To parallelize this smoothing process, a separate nodal partition is generated such that every surface node involved in the NBS grid generation is owned by only one processor. For each smoothing step, a box filter is applied to the current extrusion height set at each node followed by a nodal exchange of the node extrusion heights to all neighboring processors. This smoothing is iterated for a set number of user-defined steps to achieve smooth grid transitions across the NBS.

Automatic mesh generation around complex vehicles would require more sophisticated grid generation algorithms such as node normal smoothing as shown by Meakin [2] et al. or the hyperbolic mesh marching method as shown by Secco et al. [22].

3.3. *NBS-Cart parallelization*

The NBS solver first identifies all surface elements contained within the fluid domain and then partitions the grid based on the surface mesh. Partitioning is performed using the METIS library with a k-way partitioning approach to maintain good load balancing across all processors [23]. The NBS and Cartesian solvers are solved in a sequential manner and so the NBS partitioning occurs across all processors being used for a given simulation. The overset interpolation algorithm (shown next) is performed on the surface partition computed by METIS due to better load balancing than the volume-based surface partition from the Cartesian solver. Only a fraction of the processors on the Cartesian volume partition touch the surface, hence, any manipulation of solution data near the surface is better handled by the NBS partition. Data transfers between the two solvers may then exchange data between the two partitions for purposes of a fully parallelized solution coupling. A schematic of a sample surface partition using METIS is shown in Fig. 6 for a 10 processor grid on the fore-body of the MSL capsule.

Once each processor has been given a list of surface elements that it now owns (shown as blue cells in Fig. 6), the process of generating the grid data structure can proceed. This begins first with the identification of two layers of neighboring elements on the surface grid and the differentiation of these cells between domain boundary surface elements and exchange elements (elements owned by other processors). Upon identification of the complete list of cells (interior, exchange, and domain boundary if any), each processor generates its own local grid based on the computed variable extrusion height. Next, the unique

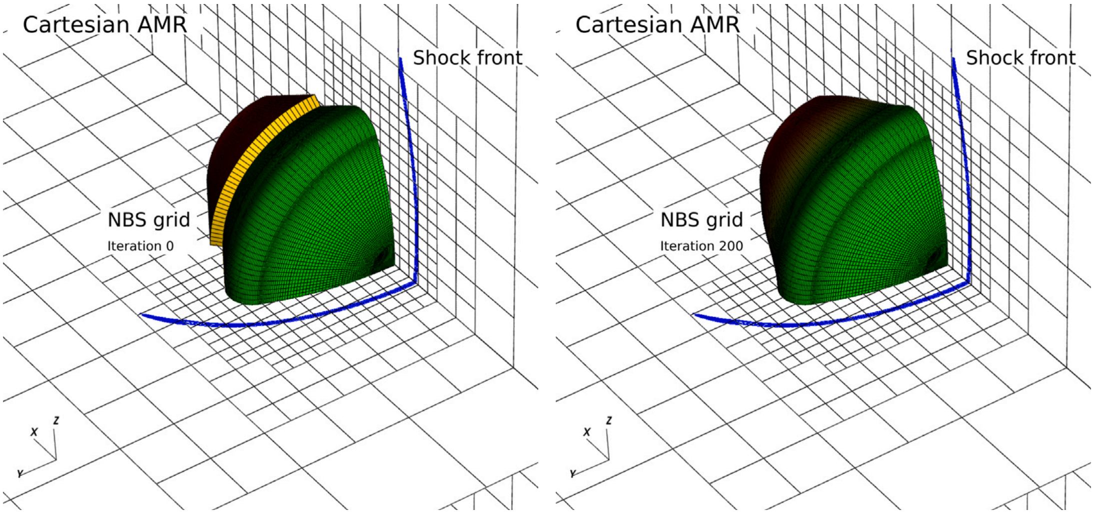

Fig. 5. NBS grid extrusion procedure starting with identification of local ray extrusion height as a function of local Cartesian cell size (left) followed by 200 extrusion smoothing steps using neighboring rays (right). NBS grid colored by extrusion height.

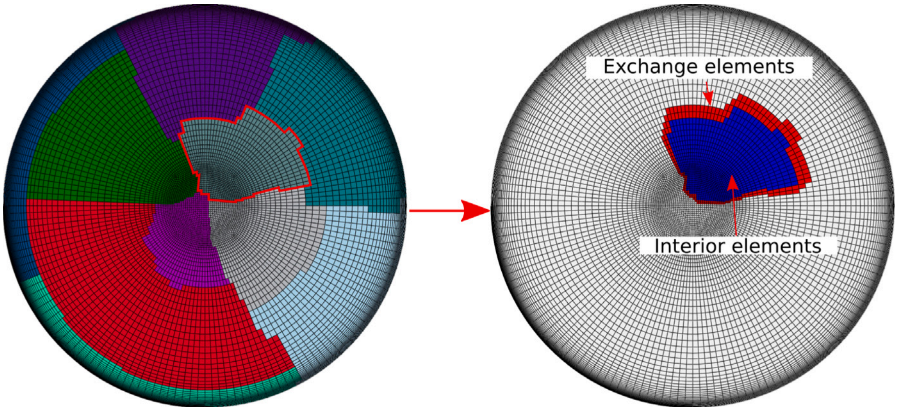

Fig. 6. NBS surface partition for the MSL capsule on 10 processors with the right image depicting a single processor zone with its interior elements marked in blue and exchange elements marked in red.

numbering of all local partition nodes, faces and cells is performed as well as the necessary computation of relevant geometric quantities of all faces and cells and the associated point clouds for computing finite volume cell and face gradients.

3.4. NBS overset interface

The coupling of the Cartesian off-body solution to the NBS overset boundary condition located at each ray tip is applied through image points. From each surface element centroid, image points are projected along the surface element normal for a distance equal to the height of the NBS grid extrusion. This places the image points directly on the shared face between the last interior cell of each surface ray and the first guard cell at the NBS overset interface (Fig. 7). A surface ray is denoted as the collection of wall-normal cells protruding from a given surface element. The flow-field at the image points is sampled from the surrounding Cartesian cells using a weighted least-squares (WLSQR) interpolation with the weighting being based on the distance from the Cartesian cell to the image point. The NBS in this work is used to resolve the entire boundary layer which implies that the NBS overset interface is located beyond the boundary layer edge. For all cases shown in this work, the image point interpolation requires only second order accuracy since the image points are located within smooth flow regions. Higher order accuracy has negligible impact on the final solution for the cases tested in this work.

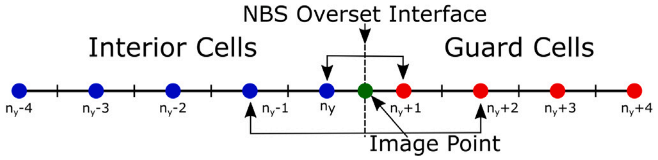

Fig. 7. NBS 1D stencil schematic of grid cells located within the vicinity of the overset interface as well as the location of the Cartesian grid image point with n_y denoting the number of wall-normal cells.

Due to the partitioning strategy employed on the Cartesian grid, not all processors own surface elements, hence, the volume-based surface partition of the Cartesian solver and that of the NBS rarely align. Fig. 8(a) shows the volume-based surface partition which clearly follows a block-structured topology and also highlights the idea that not all processors own surface elements. Every surface element has an associated image point which can be used to set boundary conditions (for IBM simulations) or NBS overset interface conditions (for the NBS-Cart solver) with the ownership of the image point data being represented by the Cartesian surface partition. The interfacing NBS surface partition is also shown on the right in Fig. 8(b) which shows the misaligned communication structure. A communication interface is required to send the image point interpolation data from the Cartesian partition onto the NBS partition before the overset boundary condition

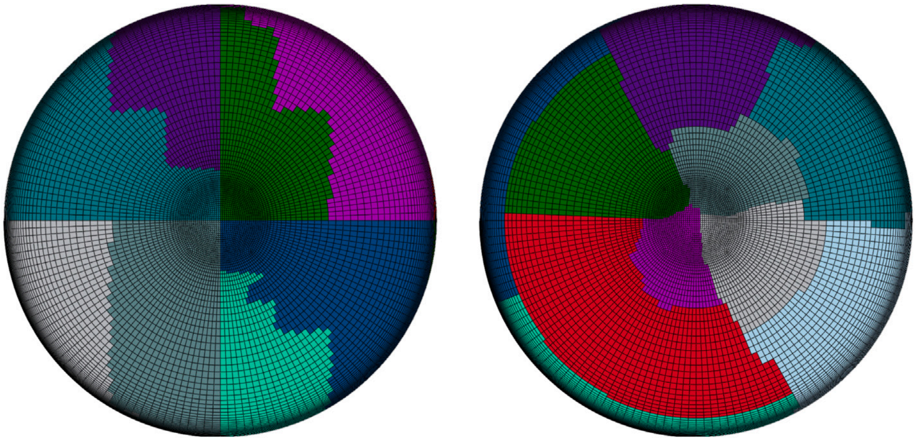

Fig. 8. Sample schematic of the volume-based surface partition of the Cartesian solver (left) and the surface partition computed with METIS for the NBS (right).

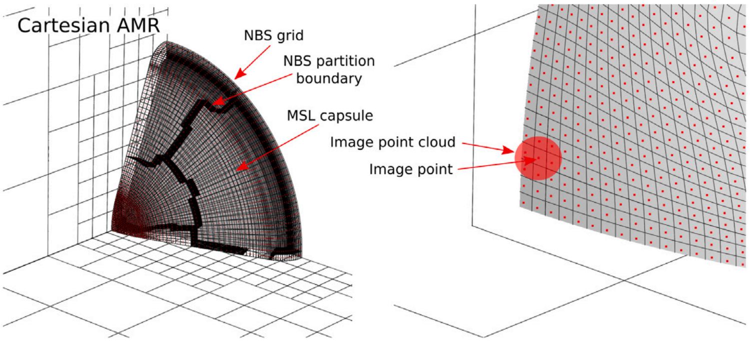

Fig. 9. NBS-Cartesian solver layout for the MSL capsule with the near body grid overlayed on top. Note that each block on the Cartesian mesh contains $n_x \times n_y \times n_z$ grid points.

can be applied. After the exchange, the overset boundary condition uses a Dirichlet condition on all quantities to fix the state at the image point quantities. The interior and image point data is used to fill each subsequent layer of guard cells using the following stencil

$$\phi_{IP} = \frac{1}{2}\left(\phi_{n_y+j} + \phi_{n_y-j+1}\right) + \mathcal{O}(\Delta x^2), \tag{15}$$

where ϕ_{IP} denotes the image point state, n_y is the number of wall-normal interior cells, and j is the guard cell layer which ranges from 1 to n_g such that n_g is the number of guard cells required to satisfy the interior scheme order of accuracy. The use of this stencil is made possible due to the mirroring of the cell sizes over the overset interface as previously described which also helps to enhance the NBS robustness versus a non-uniform stencil. The complete Cartesian to NBS overset interface coupling may then be shown in Fig. 9. Similarly, the red points in Fig. 9 denote image points at the NBS overset interface and the shaded red region refers to the image point interpolation cloud used to sample the Cartesian volume solution for application of the NBS overset boundary condition.

3.5. Overset interpolation algorithm

The use of an NBS negates the need for an immersed boundary for the Cartesian grid solver because of the use of an overset interpolation algorithm. The near-wall Cartesian flow-field is set via an overset interpolation from the NBS solution into several layers of Cartesian cells which removes the need for high levels of grid resolution on the Cartesian grid. Furthermore, no irregular schemes are required on the Cartesian solver which helps alleviate robustness and accuracy issues typically found in the vicinity of immersed boundaries.

The overset interpolation begins by identifying an upper and lower bound for the overset region on the Cartesian grid. The lower bound in this work is taken as the geometric surface position while the upper bound is located approximately $n\Delta x$ away from the lower bound such that Δx is the local minimum grid spacing near the surface. The upper bound is not taken as a fixed limit for this overset algorithm; its primary purpose is for visualization of the underlying methodology. It is shown in Fig. 10(a) that in regions of no grid alignment with the boundary, all required overset cells are clustered well below the approximate upper bound than regions of increased grid-boundary alignment. Four layers of cells are employed to ensure no regular convective stencils attempt to access data stored in invalid cells behind the boundary.

Upon identification of all overset Cartesian cells, each cell must be mapped to an NBS donor point. An NBS donor point is defined as the NBS cell center that has been associated with a given overset cell and will be used as the central point in the overset interpolation cloud, from which all remaining cloud points will be referenced to. To identify the donor point for each overset cell, a kd-tree is built from the surface grid. Then, each overset cell identifies the nearest n surface elements as potential candidates as shown in Fig. 10(b) for a sample three point nearest neighbor identification. Each candidate is then checked to ensure it resides within the NBS fluid domain. Multiple candidates are identified from the kd-tree to ensure we fine the closest in-domain element, since for more complicated geometries, the closest surface centroid is not necessarily equivalent to the closest in-domain surface centroid. The partitioning of the overset interpolation is based on which candidate surface element each overset cell selects. In general, all processors claim a subset of the overset Cartesian cells to interpolate into (based on the NBS surface partition), however, this distribution is rarely perfectly load balanced. The overall cost of this interpolation is negligible in comparison to other more intensive operations (such as right-hand side evaluations or implicit solves) and so the efficiency of this algorithm is acceptable.

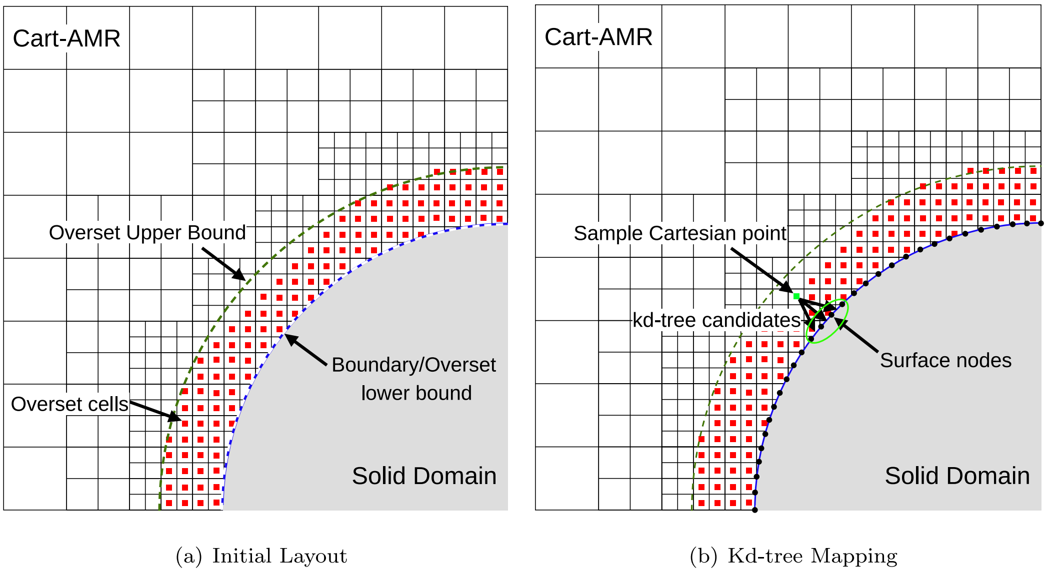

(a) Initial Layout (b) Kd-tree Mapping

Fig. 10. Overset Cartesian cell map showing all identified overset Cartesian cells (left) and a sample 3-point kd-tree mapping approach for the green overset cell to identify the closest in-domain surface element.

The final step of the overset interpolation setup after the overset cells have selected a candidate surface element, and hence partitioned themselves, a 1D look-up operation is performed to find the NBS donor point. This operation is performed by comparing the distance function of the Cartesian cell and all wall-normal NBS cells associated with this surface element to find the nearest NBS cell center on this ray. With an identified donor point, a cloud of cells built from three wall-normal layers of the NBS grid is built (with the NBS donor as the central layer). The number of points in the cloud is a function of the number of neighbors a given cell has. In this work, quadrilateral surface elements are used which have eight neighbors within a given NBS layer (including diagonal neighbors) for a total of 27 NBS points in the interpolation cloud. Interpolation coefficients are computed using a second order WLSQR routine, similar to the overset interface.

For perfect gas simulations, the primitive variables are interpolated into each Cartesian cell, whereas for high-enthalpy cases, the solver interpolates the fluid pressure, $ns - 1$ mass fractions, velocities, and temperatures onto each Cartesian cell. From this interpolated state, the species densities may be computed. The final species density for species ns can be reconstructed from the interpolated pressure, temperature, and the other $ns - 1$ mass fractions. Interpolating pressure and mass fractions as opposed to species densities reduces pressure artifacts in the Cartesian flow-field that appear immediately after the interpolation due to difficulties in accurately capturing the strong species density gradients in the near-wall region and helps to enhance solver robustness and stability. It has been noted by the authors that pressure oscillations (resulting from the overset interpolation) have a much more significant impact on solver stability than oscillations in other quantities. It is assumed that the pressure generally sees more significant interpolation errors than other quantities when using the primitive state since the interpolation error from all the species densities and temperature would be cumulative when computing the mixture pressure with $p = \sum_{s=1}^{ns} \rho_s R_s T$ versus directly interpolating pressure. For the 3D cases studied in this work, artifacts caused by the overset interpolation algorithm are not a concern. Artifacts are only realized when interpolating within the boundary layer, however, for all cases in this work, the Cartesian cell size at the surface is larger than the local boundary layer thickness resulting in the interpolation happening in low-gradient regions. However, to demonstrate this issue, a sample 2D reentry capsule at Mach 7.9 is simulated such that the Cartesian grid may be refined sufficiently until the first few layers of cells at the surface reside inside the boundary layer.

Fig. 11 shows the comparison of directly interpolating the mixture pressure near the wall and reconstructing the mixture pressure at the wall using the interpolated primitive variables. Clear pressure artifacts are shown within the first layer of cells at the surface when trying to reconstruct the pressure using the interpolated primitive variables. By directly interpolating the pressure into these cells, the pressure artifacts are completely removed. The interpolation of other variables within the near wall region are shown in Fig. 12. Minimal artifacts are shown in the velocity contours, however, interpolation errors are picked up in the mass fraction and temperature values in the first two layers of cells. This Cartesian grid is over-resolved for this 2D test case which leads to the overset interpolation occurring deep into the boundary layer whereas a typical 2D test case would use coarser grid cells at the surface to avoid this issue and still be able to obtain a grid converged solution.

3.6. NBS extrusion limitations

The user specified settings that control the NBS grid generation are a function of the freestream conditions and of the coupling methodology. The number of wall-normal cells and the cell size at the surface of the NBS is determined based on the required boundary layer resolution to achieve grid convergence and based on the cell Reynolds number, respectively. The final variable is the NBS extrusion height, however, which is dependent on the employed coupling methodology and in particular, the local Cartesian cell size in the vicinity of the NBS grid. It is easier to discuss the extrusion factor, α, instead of an extrusion height, h_{NBS}, such that the extrusion factor in 1D may be defined as

$$\alpha = \frac{h_{NBS}}{\Delta x_{Cart}}, \tag{16}$$

where Δx_{Cart} is the local Cartesian grid spacing at the wall. To maintain solver stability, a lower bound on the NBS extrusion height must be set such that well-posed overset interpolation stencils may be found which do not access data stored in the NBS guard cells at the overset interface. By avoiding any data access from the NBS overset interface guards, the Cartesian and NBS solutions allow for some feedback and stabilization to occur between the competing fluid solutions which becomes especially important in subsonic regions as seen behind detached shock structures from the various cases shown later in this work.

In general, the minimum extrusion factor that is capable of retaining a stable coupling is around 4 based on the test cases used in this

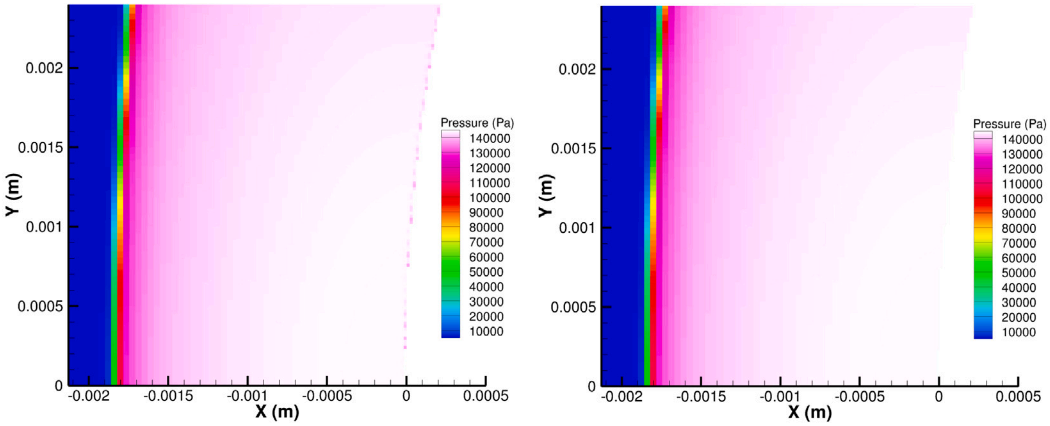

Fig. 11. Close-up of the mixture pressure flow-field in the nose region of a Mach 7.9 re-entry capsule showing the overset interpolated state via reconstructing the pressure (left) and via interpolating the pressure directly (right).

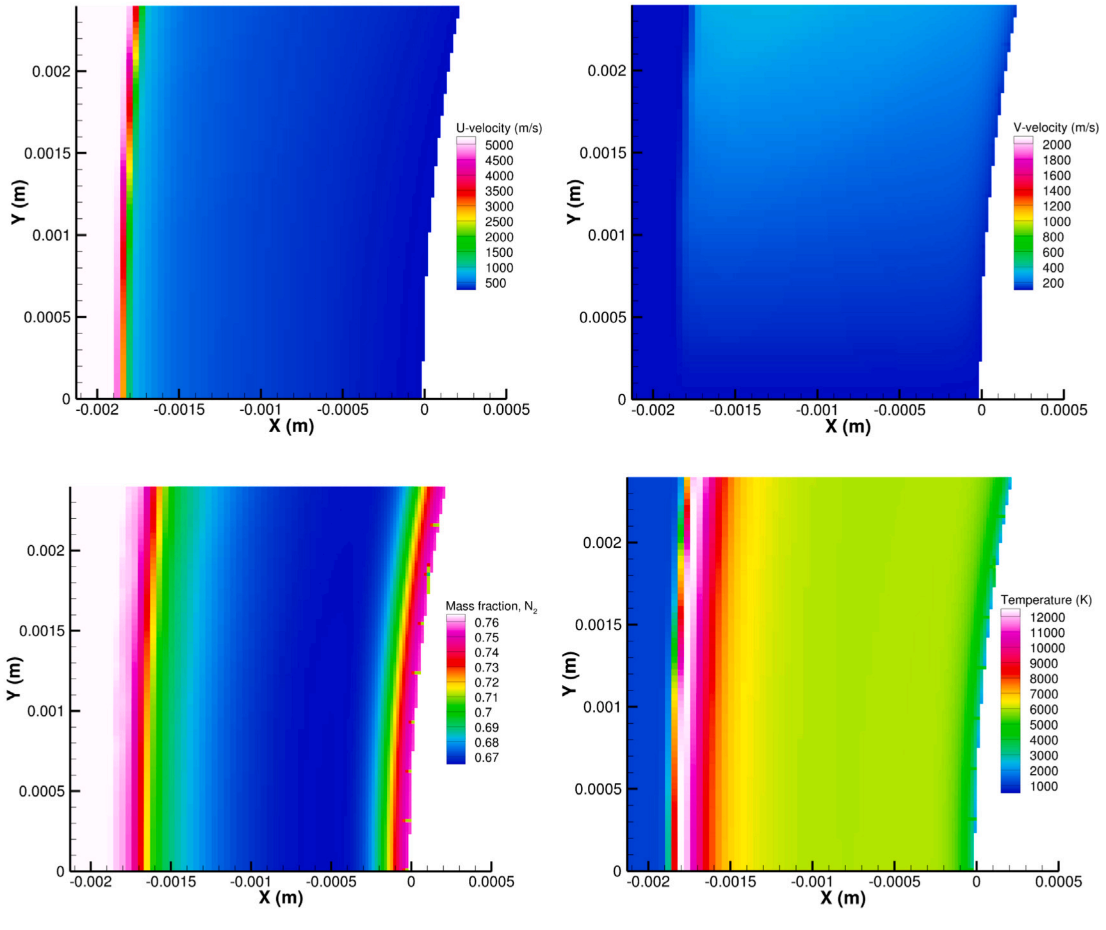

Fig. 12. Close-up of various interpolated quantities in the near-wall region of a Mach 7.9 re-entry capsule to highlight overset interpolation difficulties in high-gradient regions.

work. The upper bound on the extrusion factor is arbitrary, however, a smaller extrusion factor requires less wall-normal cells to achieve grid convergence on the NBS. For multi-dimensional flows, the lack of a wall-aligned Cartesian grid needs to be accounted for when computing the extrusion height and so Δx_{Cart} is replaced with $\Delta \tilde{x}_{Cart}$ which represents the cell diagonal length of the Cartesian cell near the wall. For 3D flows, this is given as

$$\alpha = \frac{h_{NBS}}{\Delta \tilde{x}_{Cart}} = \frac{h_{NBS}}{\sqrt{\Delta x_{Cart}^2 + \Delta y_{Cart}^2 + \Delta z_{Cart}^2}}. \tag{17}$$

Based on the test cases in this work, an extrusion factor between 4 and 6 yielded good accuracy and stability. For the MSL and Orion test cases, an extrusion factor of 6 was used while an extrusion factor of 4 was used in the AS-202 capsule due to the smaller shock standoff distance. Allowing the shock to interact with the NBS overset boundary condition can pose stability issues and so this interaction is avoided in this work.

3.7. Cartesian adaptive mesh refinement

The Cartesian solver grid generation employs an adaptive mesh refinement algorithm (AMR) when CHAMPS initializes to automatically generate a grid based on the user provided settings. Different regions of an imported geometry can be assigned a different identifying component number (set within the mesh generation program, i.e. Pointwise in this work). The user may then specify different target grid resolutions for each component number on the Cartesian grid. The AMR algorithm will then recursively split blocks isotropically in all three dimensions until the target grid resolution is achieved. This generated block topology represents the initial Cartesian grid for a given simulation. During runtime, the AMR is periodically called (at a user-specified frequency) to locally identify blocks for refinement or derefinement as the flow-field evolves. The refinement strategy may be based on any number of target criteria, however, only two are used in this work.

The Cartesian AMR does flow feature refinement via pressure gradient tracking. A refinement function, Ψ, is defined as

$$\Psi = \frac{\nabla p}{\max|_{\Omega}\left(\nabla p\right)}. \tag{18}$$

With the normalized pressure gradient across the entire block-structured Cartesian grid, AMR refinement and derefinement is handled based on user provided threshold values such that if $\Psi < \Psi_l$ is true for any point in a block, the block is coarsened while if $\Psi > \Psi_u$, the block is refined with refinement taking priority over derefinement [24]. To remove any influence of the grid spacing on the computed pressure gradient, the lower and upper bounds on the refinement function are scaled based on the grid level

$$\left.\begin{aligned} \Psi_l^n &= \frac{1}{2^{L_{max}-n}}\Psi_l \\ \Psi_u^n &= \frac{1}{2^{L_{max}-n}}\Psi_u \end{aligned}\right\} \text{with n} \in [1,\ L_{max}]\ . \tag{19}$$

Ψ_l^n and Ψ_u^n represent the respective lower and upper bound AMR thresholds scaled for a given grid level n and L_{max} is the user set maximum number of refinement levels. In this work, the lower and upper bound on the refinement function has been set to 0.05 and 0.1, respectively.

To facilitate wake tracking in the AS-202 capsule (shown later), an additional refinement criteria is added in to track subsonic flow regions and apply targeted refinement. The AMR computes the Mach number in all grid cells and any block which is found to contain subsonic flow regions is refined up to a user-specified maximum refinement level L_{max}^w where $L_{max}^w \leq L_{max}$.

3.8. Spatial and temporal discretization schemes

The CHAMPS block-structured Cartesian solver in this work uses the WENO-Z scheme of Jiang and Shu [25] with smoothness indicators proposed by Liu et al. [26]. It was shown in Ref. [27] that WENO-Z provides a good compromise between accuracy and cost; it eliminates order reduction at critical points, but it is more expensive than a mapped WENO scheme. The smoothness indicators detect local discontinuities and reduce the formal order of accuracy to a third order scheme. For flow-fields with strong shocks on non-aligned grids, even the reduced order WENO scheme can produce pre- and post-shock artifacts and so the WENO scheme is augmented with a characteristic variable reconstruction based on the Roe-averaged state and the convective flux is computed with Steger–Warming flux splitting which is employed for all cases in this work. On non-aligned grids, shock artifacts can present themselves under certain conditions which impact the accuracy of the heat flux profile on the surface. This issue is corrected by fully reducing to a first order convective scheme in the presence of strong shocks. This is achieved by using the classical Ducros sensor [28] to formulate a numerical flux as

$$\hat{f}|_{i+1/2} = (1-\tilde{\alpha})\hat{f}|_{i+1/2}^{WENO} + \tilde{\alpha}\hat{f}|_{i+1/2}^{O1}, \tag{20}$$

where $\tilde{\alpha}$ is the Ducros sensor value, $\hat{f}|_{i+1/2}^{O1}$ is the right face flux computed using a first order scheme and $\hat{f}|_{i+1/2}^{WENO}$ is the right face flux computed using a fifth order WENO flux reconstruction with characteristic variable transformation. The scheme is able to efficiently detect shocks and remove artifacts that would otherwise deteriorate the predicted heat flux profile with a minimal increase in computational overhead.

The NBS solver uses a finite-volume formulation with a third order MUSCL reconstruction [29] to obtain the left and right flow states on a given face with the convective flux being computed with a modified Steger–Warming flux function to reduce dissipation within the boundary layer. The left and right states at the face are reconstructed as

$$q_{i+1/2}^L = q_i + \frac{1}{4}\left[(1-\kappa)\phi(\Delta r_i)\left(q_i - q_{i-1}\right) + (1+\kappa)\phi(\nabla r_i)\left(q_{i+1} - q_i\right)\right] \tag{21}$$

and

$$\begin{aligned} q_{i+1/2}^R = q_{i+1} - \frac{1}{4}\Bigg[&(1-\kappa)\phi(\nabla r_{i+1})\left(q_{i+2} - q_{i+1}\right) \\ &+ (1+\kappa)\phi(\Delta r_{i+1})\left(q_{i+2} - q_{i+1}\right)\Bigg], \end{aligned} \tag{22}$$

where $\phi(r_i)$ is a flux limiter to handle non-smooth solution reconstructions and κ controls the order of accuracy on the solution reconstruction. Setting $\kappa = -1$ yields a second order scheme while $\kappa = 1/3$ yields a third order scheme (which is the method used in this work). A minmod style limiter is employed where

$$\phi\left(\Delta r_i\right) = \max\left(0, \min\left(1, \frac{q_{i+1} - q_i}{q_i - q_{i-1}}\right)\right) \tag{23}$$

and

$$\phi\left(\nabla r_i\right) = \max\left(0, \min\left(1, \frac{q_i - q_{i-1}}{q_{i+1} - q_i}\right)\right). \tag{24}$$

The formulation of the modified Steger–Warming flux is detailed next. The Steger–Warming scheme employs a flux splitting approach into upwind and downwind components as

$$\hat{f}|_{i+1/2} = A_i^+ q_{i+1/2}^L + A_{i+1}^- q_{i+1/2}^R, \tag{25}$$

where $A = \frac{\partial F}{\partial \eta}$ is a diagonalizable Jacobian matrix of the convective flux, F, in the face normal direction, η, evaluated at the cell center. The splitting of matrix A into its upwind and downwind components is performed as

$$A^{\pm} = R\Lambda^{\pm}L, \tag{26}$$

where R is the matrix of right eigenvectors of A and L is the inverse of R. Appendix D gives the left and right eigenvector matrices used for the perfect gas simulations while Appendix E gives the matrices for the TCNE solver. Steger and Warming [30] proposed eigenvalues of the form

$$\lambda_i^{\pm} = \frac{1}{2}\left(\lambda_i \pm \sqrt{\lambda_i^2 + \epsilon^2}\right) \tag{27}$$

where $\lambda_i = \{\hat{u}, \ldots, \hat{u}, \hat{u}+a, \hat{u}-a, \hat{u}\}^T$ is the eigenvalue vector for the TCNE convective flux, $\lambda_i = \{\hat{u}, \hat{u}, \hat{u}, \hat{u}+a, \hat{u}-a\}^T$ is the eigenvalue vector for the perfect gas convective flux, and ϵ is used to add dissipation into the flux scheme as

$$\epsilon = 0.3\left(|\hat{u}| + a\right). \tag{28}$$

The modified Steger–Warming scheme shifts the evaluation of $A^{\pm}$ onto the cell face and computes the matrix using an averaged state q_a. The modified scheme needs to revert to the original formulation (matrix evaluation at the cell center) when approaching discontinuities to maintain stability. Therefore, a switching of the form

$$q_a^+ = (1-w)\,q_{i+1/2}^L + w q_{i+1/2}^R \tag{29}$$

and

$$q_a^- = w q_{i+1/2}^L + (1-w)\,q_{i+1/2}^R, \tag{30}$$

where $q_a^{\pm}$ is used to compute $A^{\pm}$ and w is a shock sensor given as

$$w = \frac{1}{2}\frac{1}{(\alpha \nabla p)^2 + 1} \tag{31}$$

and

$$\nabla p = \frac{|p_i - p_{i+1}|}{\min\left(p_i, p_{i+1}\right)}. \tag{32}$$

The parameter α is used to control the sensitivity of the shock sensor and is set to 6 in this work. In smooth flow regions, the shock sensor will approach 1/2 such that $A^{\pm}$ will be computed using the average of the left and right reconstructed states, while at shocks, the sensor approaches 0 such that $A^{\pm}$ is computed using the left or the right state, respectively.

Due to the discrepancy in spatial scales between the two grids, solution oscillations may exist if the respective CFL numbers differ by a significant magnitude. Therefore, the Cartesian solver is advanced with a two stage, second order RK scheme while the NBS solver takes advantage of the structured wall-normal memory layout to employ the DPLR [31] implicit algorithm for rapid convergence of the wall-normal boundary layer gradients. The NBS also solves the full set of governing equations shown in Section 2 to remain consistent with the off-body solution. The full time advancement algorithm for the NBS-Cart solver is given in algorithm 1.

Algorithm 1 NBS-Cart solution advancement procedure

```
Interpolate to Cartesian solver image points.
Cartesian to NBS partition exchange of image point data.
Set boundary conditions on NBS.
Solve governing equations on NBS and advance solution forward in time.
Compute surface data on NBS (if this is an output step).
Overset interpolation of NBS near-wall flow-field onto Cartesian overset cells.
NBS to Cartesian partition exchange of overset cell data.
Apply overset cell interpolation onto relevant Cartesian cells.
Set boundary conditions on Cartesian solver
Advance Cartesian solver forward in time.
```

4. CHAMPS NBS-Cart solver validation

Validation of the CHAMPS NBS-Cart solver will be shown for both perfect gas and high-enthalpy flows for various capsule geometries at non-zero angles of attack. The perfect gas NBS-Cart solver is validated using a scale Mars Science Lander (MSL) capsule against experimental and numerical data for surface heat flux measurements along the capsule center line for a range of angles of attack from 0-degrees to 16-degrees. Additional validation of the perfect gas solver is then performed on the Orion Crew Exploration Vehicle (CEV) at higher angles of attack of 16–32 degrees. Validation of the Orion CEV is achieved via comparison to published experimental results and the numerical solution from LAURA for surface pressure and heat flux on the fore-body. The TCNE NBS-Cart solver in this work is validated on the AS-202 capsule against the solution from DPLR for a single trajectory point at an angle of attack of 17.8 degrees as well as against available flight data.

4.1. Case 1 - Mach 9.47 MSL Capsule

Validation of the formulated NBS-Cart solver for low-enthalpy flows is performed on a scale MSL capsule at various angles of attack ranging from 0–16-degrees in increments of 4-degrees. This allows for validation of the heat flux prediction capabilities for complex flow fields of a capsule at non-zero angles of attack. The MSL capsule is tested at Mach 9.47 and was initially run experimentally by Hollis and Collier (2008) [32], namely run 3021 which is the lowest Reynolds number case to maintain laminar flow on the capsule fore-body. Numerical results are also available from the work of Chen et al. [33] using a body-fitted solver. Freestream conditions for this case are provided in Table 1.

Table 1
Freestream conditions for the Mach 9.47 MSL capsule test case.

p_∞ (Pa)	u_∞ (m/s)	T_∞ (K)	T_w (K)	Ma	Re_∞ (1/m)
167.9	1405.59	54.8	294.44	9.47	4.32×10^6

A surface grid is generated for the MSL capsule which is provided to the NBS-Cart solver for generation of the NBS and Cartesian volume grids during start-up. A 180-degree capsule section of the fore-body is simulated to capture the angle of attack effects on the surface heating and since no side-slip angle was measured in the experimental campaign. The 0-degree angle of attack, however, employed only a 90-degree section of the capsule. A visualization of the employed surface grid for the MSL capsule as well as the overall NBS-Cart grid structure is shown in Fig. 13. The surface grid is entirely composed of quadrilateral elements and the NBS extrusion is performed well into the shock layer to facilitate the coupling between both solvers.

Initial analysis of this test case is targeting the impact of the Cartesian convective scheme treatment on the computed surface heating profile while the NBS convective scheme treatment remains fixed (employing a 3rd order MUSCL scheme with a modified Steger–Warming flux). Four methods are tested on the Cartesian solver. Method 1 employs a WENO-Z scheme with a Rusanov flux splitting as shown in Eq. (33)

$$\hat{\boldsymbol{f}}_i^{\pm} = \boldsymbol{f}_i \pm \lambda_i \boldsymbol{U}_i, \tag{33}$$

while method 2 employs a global Rusanov flux splitting in the WENO-Z scheme such that λ is taken as the maximum value of the spectral radius across the entire WENO-Z stencil as in Eqs. (34) and (35) (as suggested in Shu and Osher [34])

$$\hat{\boldsymbol{f}}_i^{+} = \boldsymbol{f}_i + \max(\lambda)_{i-2:i+2}\boldsymbol{U}_i \tag{34}$$

and

$$\hat{\boldsymbol{f}}_i^{-} = \boldsymbol{f}_i - \max(\lambda)_{i-1:i+3}\boldsymbol{U}_i. \tag{35}$$

Method 3 employs a Steger–Warming flux with the WENO-Z scheme while method 4 employs the method presented in Section 3.8 which employs a Ducros sensor for shock detection and locally reduces the WENO-Z scheme to a first order numerical scheme at the shock front. Fig. 14 shows the computed heat flux profile on the MSL capsule at an 8-degree angle of attack since this angle of attack was the most challenging for the Cartesian solver to obtain artifact free heating profiles. Also shown is the U-velocity contour extracted at the symmetry plane of the capsule to highlight the incoming velocity streaks generated at the shock front while using higher order methods in this region (methods 1–3).

Methods 1–3 show velocity streaks coming in from the shock which then get interpolated to the NBS interface and imprint themselves onto the surface which generates a significant heating artifact. The Ducros sensor effectively identifies the shock front and reduces the WENO-Z scheme to a first order treatment and removes any velocity streaks from negatively impacting the surface solution, although it does produce a slightly more diffused shock. It is assumed that this issue is a result of the Cartesian grid not being aligned with the shock front as is typically done for body-fitted codes to avoid numerical artifacts. Therefore, all subsequent results will employ method 4 as previously mentioned.

Validation of the solver is limited to surface heating extracted along the symmetry plane to compare both the windward and leeward side heating on the fore-body only. A grid convergence study was

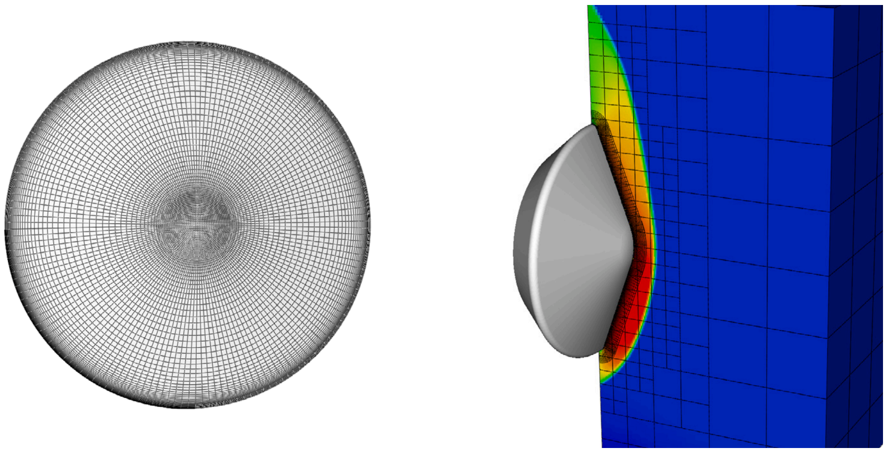

(a) Surface Grid (b) NBS-Cart

Fig. 13. NBS-Cart computational model schematic for the MSL capsule at a 16-degree angle of attack. The MSL capsule and surface grid is visualized (left) as well as the NBS volume mesh and Cartesian block-structure with the Cartesian domain colored by temperature (right).

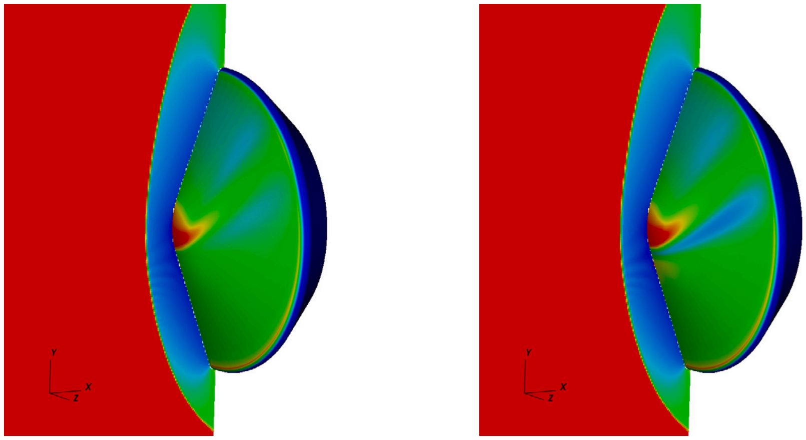

(a) Method 1 (b) Method 2

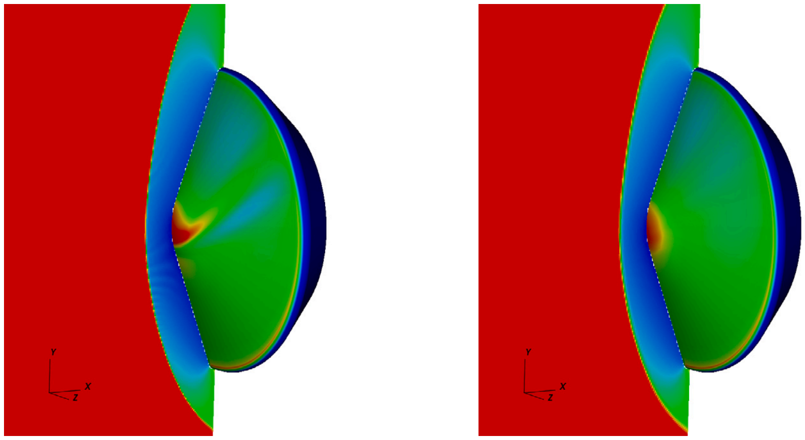

(c) Method 3 (d) Method 4

Fig. 14. Comparison of various Cartesian solver convective scheme treatments in terms of computed U-velocity contours and surface heat flux profiles at an 8-degree angle of attack on the MSL capsule.

performed at the highest angle of attack. The Cartesian grid for each case employed roughly 2.5 million cells with a cell size of $\Delta x = 8.33 \times 10^{-4}$ m at the surface. The NBS grid used for the results in this section (upon conclusion of the grid study) used 100 points in the wall-normal direction and about 5200 cells on the capsule surface for a total of 500k cells. The cell size at the wall was held at $\Delta x = 1 \times 10^{-6}$ m. The total combined cost of each case was around 3 million points with the 0-degree model employing half as many points due

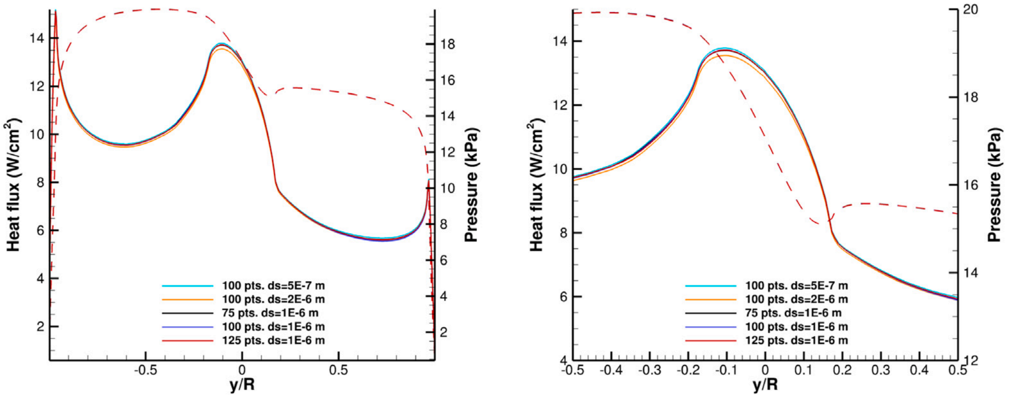

Fig. 15. Heat flux profile along XY plane for the MSL capsule at 16-degrees from the NBS grid resolution study (left) with a close-up view at the nose (right). Solid lines denote heat flux profiles while dashed lines denote pressure profiles.

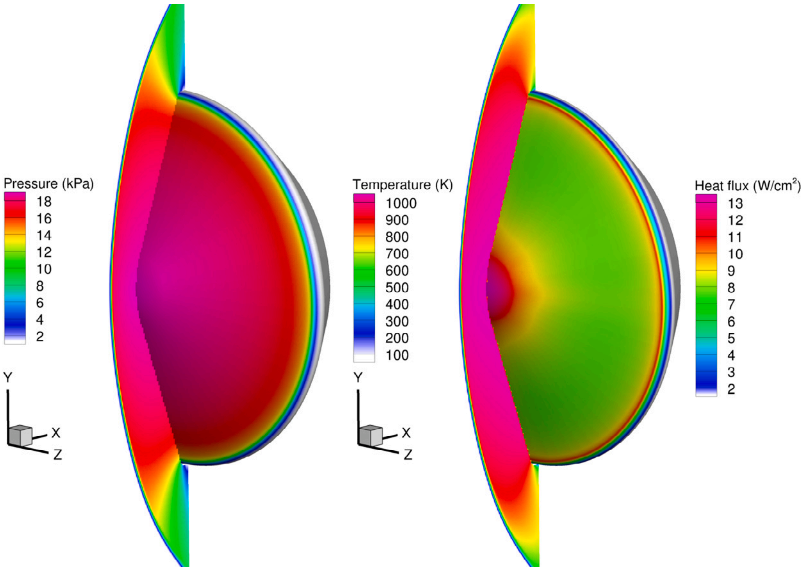

(a) Surface Pressure (b) Surface heat flux

Fig. 16. Surface pressure and heat flux profiles on the MSL capsule at Mach 9.47 and a 0-degree angle of attack.

to the use of a 90-degree section. The results from the grid study at the 16-degree angle of attack condition is shown in Fig. 15 with the solid and dashed lines representing the heat flux and pressure profiles, respectively. Good grid convergence is achieved for all cases in terms of the surface pressure profile. Focusing exclusively on the prediction of the stagnation point heating, slight differences are noticed upon reducing the cell size at the surface with $\Delta x = 2 \times 10^{-6}$ m under-predicting the magnitude by a small amount, however, smaller cell sizes of $\Delta x = 1{\times}10^{-6}$ m and $\Delta x = 5{\times}10^{-7}$ m show good agreement. In terms of wall-normal resolution, no variation in heating is shown, demonstrating grid convergence. Therefore, the NBS grid with 100 wall-normal points and a cell size of $\Delta x = 1 \times 10^{-6}$ m is used for all subsequent MSL cases.

Beginning with the 0-degree angle of attack, the surface pressure and heating contours on the capsule are shown in Fig. 16.

The computed surface pressure contour shows a peak pressure of about 20 kPa with a smooth profile as expected. The surface heating profile, shown in Fig. 16, is more sensitive to the numerical treatment and overall mesh quality of the solver, however a smooth profile is shown here as well. Looking at a profile extracted just offset from the XY plane, a comparison against published data can be made. Based on Fig. 17, good agreement is shown versus the experimental and numerical data with only a slight under-prediction of the heat flux at the stagnation point on the order of about 3%. An otherwise smooth heat flux profile is captured along the entire length of the capsule as well as an accurate capturing of the localized heating peak at the shoulders. Differences in the solution captured by the NBS-Cart solver

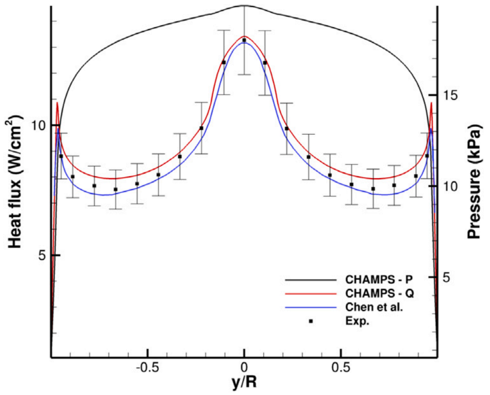

Fig. 17. Heat flux profile along XY plane for the MSL capsule at 0-degrees.

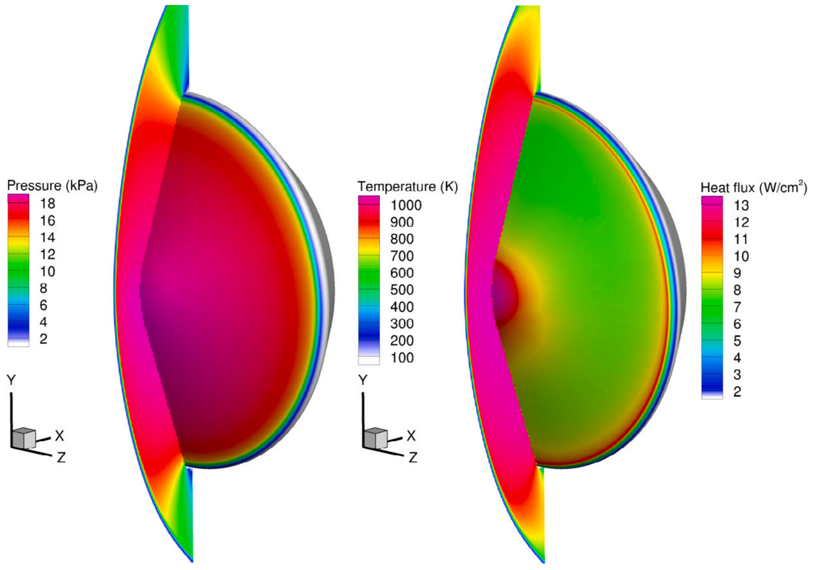

(a) Surface Pressure (b) Surface heat flux

Fig. 18. Surface pressure and heat flux profiles on the MSL capsule at Mach 9.47 and a 4-degree angle of attack.

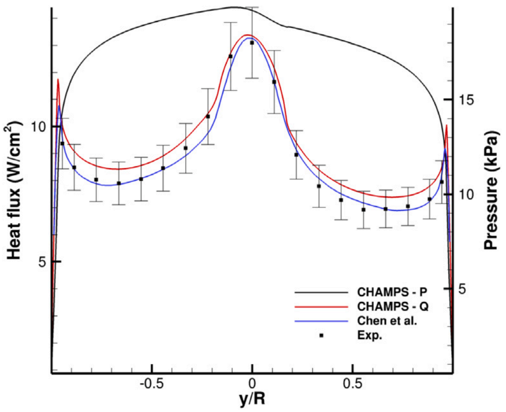

Fig. 19. Heat flux profile along XY plane for the MSL capsule at 4-degrees.

and the body-fitted results of Chen et al. [33] have been attributed to a few potential sources. One potential reason could be the reduction to a first order convective scheme used on the Cartesian solver in this work. This reduction helps to remove undesirable artifacts in the post-shock and surface solutions, however, it can cause slight adjustments to the final heating profile due to a more diffused shock front. Additionally, grid independence of the heating profile was not shown in the work of Chen et al. [33] and a cell size at the surface of $\Delta x = 5 \times 10^{-6}$ m was used which could result in an under-resolved boundary layer solution.

Moving to the 4-degree angle of attack test case, the surface pressure and heat flux profiles are shown in Fig. 18. A very slight downward shift is observed in the surface pressure profile, shifting towards the windward side of the capsule as the stagnation point shifts downwards as well. The heating profile shows reduced heating on the leeward, fore-body conical section as a result of the non-zero angle of attack and a slightly stronger heating peak on the windward shoulder than the leeward shoulder.

The slight angle of attack shifts the peak heating point onto the windward side of the capsule. Good agreement is still shown against the available experimental data and the profile remains mostly within the experimental uncertainty for the given conditions (see Fig. 19).

At 8-degrees, the surface pressure and heat flux profiles shift further towards the windward side with an increasingly large local heating peak on the windward shoulder. Some asymmetry can again be seen in the heating profile on the leeward side and windward side in the vicinity of the symmetry plane. The pressure profile is artifact free and shows a smooth surface profile as expected (see Fig. 20).

Investigating the heat flux extraction by the symmetry plane, good agreement is again shown versus the experimental and numerical data. The heat flux shows particularly good agreement on the windward side and at the stagnation point, however, a very slight over prediction is realized on the leeward side of the fore-body. The over-prediction on the leeward side has been partially attributed to the first order reduction at the shock front. A pure WENO-Z scheme on the Cartesian solver shows a heating profile that falls just below the upper uncertainty bound on the experimental data, however, a significant heating artifact manifests itself near the nose on the windward side as a result (see Fig. 21).

At 12-degrees, the shock standoff distance is significantly smaller on the windward shoulder versus the leeward shoulder resulting in a very significant increase in surface heating. The peak pressure profile has now been completely shifted onto the windward side at this angle of attack and the heat flux profile for these conditions show improved symmetry versus the 4 and 8-degree cases (see Fig. 22).

The predicted stagnation point heating is about 5% higher than that predicted by the body-fitted solution of Chen et al. [33]. Regardless, the predicted heat flux is still within experimental error from the test campaign and the local heat flux peak at the windward shoulder is now shown to be nearly equal in magnitude to the stagnation point heating (see Fig. 23).

At the final angle of attack, the relative pressure difference between the leeward and windward sides of the capsule is quite significant with the peak pressure at the stagnation point shifted a considerable distance onto the windward fore-body conical section as expected. A significant decrease in surface heating is shown on the leeward side of the capsule as the flow expands around the capsule nose resulting in a slightly thicker boundary layer (see Fig. 24).

Final comparison of this test case versus the measured experimental data shows excellent agreement in the prediction of the heat flux magnitude. For the first time, the heating at the windward shoulder shows a higher magnitude than that of the stagnation point, owing to the closeness of the shock to the surface at this flight configuration (see Fig. 25).

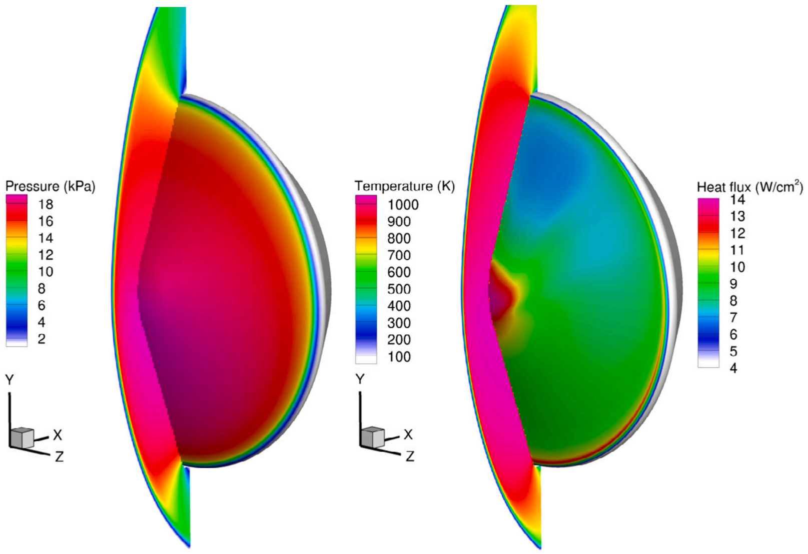

(a) Surface Pressure (b) Surface heat flux

Fig. 20. Surface pressure and heat flux profiles on the MSL capsule at Mach 9.47 and a 8-degree angle of attack.

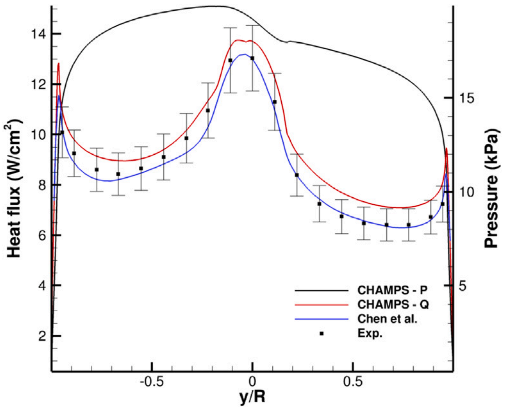

Fig. 21. Heat flux profile along XY plane for the MSL capsule at 8-degrees.

4.2. Case 2 - Mach 6 Orion CEV

The second validation case for the perfect gas 3D NBS-Cart solver involves the modeling of the Orion Crew Exploration Vehicle (CEV). A scaled down model was tested at the Langley Research Center (LaRC) 20-inch Mach 6 air tunnel at various Reynolds numbers and angles of attack. The extracted experimental data allows for validation of the surface pressure profile and surface heating of the capsule fore-body with additional numerical validation provided by Hollis using LAURA [35]. To demonstrate the capabilities of the 3D NBS-Cart solver for automatic mesh generation around the full vehicle and the capturing of the wake flow-field, a 180-degree model is simulated here including the aft-body. Geometric sizing of the capsule is provided from the work of Hollis [35].

Several Reynolds numbers based on the capsule diameter, $Re_{\infty,D}$, were simulated for each angle of attack where the capsule diameter has been scaled to 0.1778 m. At the highest $Re_{\infty,D} = 4.3 \times 10^6$, signs of transition to turbulence on the leeward fore-body were noted via a local increase in the surface heat flux. Therefore, the conditions used here are from the second highest $Re_{\infty,D} = 3.44 \times 10^6$ since validation under laminar flow conditions is sought for this work. The freestream conditions for the selected test case is given in Table 2 with the angle of attack varying from 16 to 32 degrees in 4-degree increments.

Table 2
Freestream conditions for the Mach 6 Orion CEV test case.

p_∞ (Pa)	u_∞ (m/s)	T_∞ (K)	T_w (K)	Ma	$Re_{\infty,D}$	$H_0 - H_w$ (J/kg)
1677	955.9	63.4	300	6.0	3.44×10^6	2.20×10^5

The overall grid structure employed for the Orion CEV is shown in Fig. 26. Similar to the MSL capsule, a quadrilateral surface grid is employed for this test case. The Cartesian grid is allowed to coarsen by one grid level in the aft-body region as shown through the block structure resulting in a variable NBS extrusion to be performed by CHAMPS.

A preliminary look at the converged solution for the Orion CEV capsule at a 16-degree angle of attack is shown in Fig. 27. The Cartesian AMR is used to track the shock structure in front of the fore-body of the capsule and is allowed to coarsen out beyond the shoulder extent of the CEV. The solution on the Cartesian grid is captured with a WENO-Z scheme. The wake structure also appears to be well captured, however, no heat flux and pressure measurements are available in the aft-body region and so its investigation is left as a strictly qualitative insight for this case.

The comparison of the heat flux data has been normalized using the laminar heating correlation of $St(Re_{\infty,D})^{1/2}$ which is a function of the Stanton number, St, and the Reynolds number based on the capsule diameter to be consistent with the published data of Hollis [35]. The Reynolds number used for normalization has been provided in Table 2. The Stanton number is computed as

$$St = \frac{q_w}{\rho_\infty u_\infty \left(H_0 - H_w\right)}, \tag{36}$$

where q_w is the wall heat flux, and $H_0 - H_w$ is the difference between the total enthalpy and the wall enthalpy. This value was provided by Hollis [35] for each set of experimental conditions and has also been provided in Table 2.

For the Cartesian grid, the cell size at the surface was set to around $\Delta x = 7.8 \times 10^{-4}$ m on the fore-body and $\Delta x = 1.56 \times 10^{-3}$ on the aft-body for all cases shown here. The total number of grid points is case-dependent due to the changing shock shape in combination with

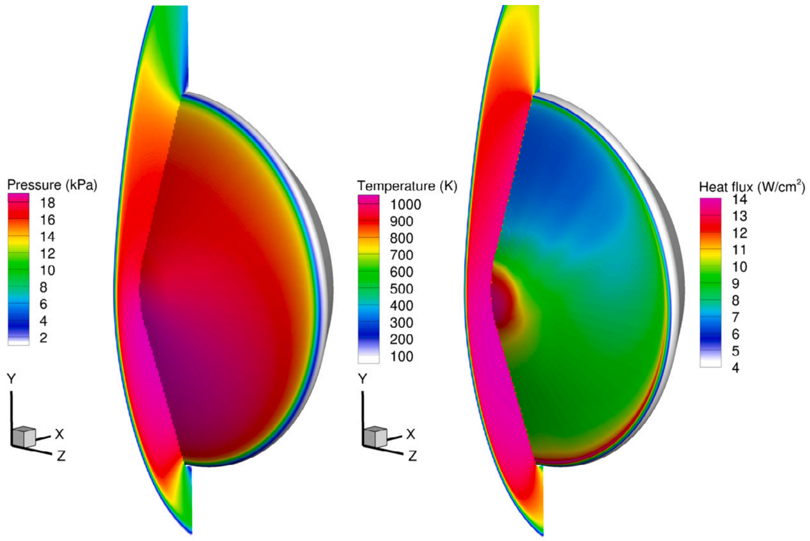

(a) Surface Pressure (b) Surface heat flux

Fig. 22. Surface pressure and heat flux profiles on the MSL capsule at Mach 9.47 and a 12-degree angle of attack.

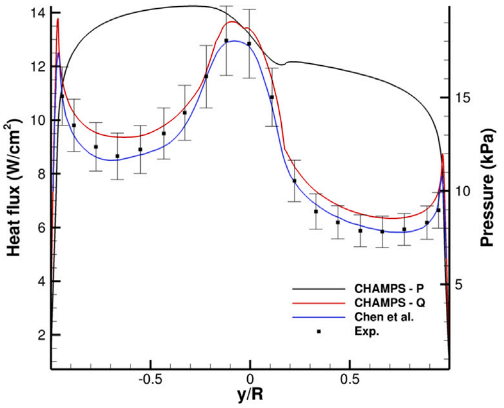

Fig. 23. Heat flux profile along XY plane for the MSL capsule at 12-degrees.

the AMR tracking, however, each case contained roughly 10 million Cartesian points.

To gauge the correct grid resolution required for an accurate prediction of the boundary layer solution, a grid study is performed on the NBS grid. The Cartesian grid resolution is assumed to have minimal impact on the fore-body heating profile provided that sufficient resolution is employed to allow for the NBS extrusion procedure to be performed. The NBS grid study was focused on the effects of the wall-normal resolution and of the cell size at the surface, whereas, the streamwise spacing is assumed to have a relatively negligible impact. Five grids were tested as shown in Fig. 28 where solid lines denote heat flux profiles and dashed lines denote pressure profiles. Both the surface pressure and surface heat flux were insensitive to variations in the wall-normal resolution and first cell size showing great grid convergence. Therefore, the final NBS grid employed a wall spacing of $\Delta x = 1 \times 10^{-6}$ m with 100 wall normal points and 16,640 points on the surface for a total grid size of 1.7 million. In total, each Orion CEV test case involved roughly 11.7 million grid points to capture a 180-degree section of the capsule.

Looking at the computed surface data for all test cases, plots of surface pressure and heat flux for the fore-body are provided in Fig. 29. The error associated with the heat flux measurements on the experimental model had been estimated to be ± 12% [35]. Comparison of the surface pressure agrees very well against the solution with LAURA. Similarly, good agreement is shown on the computed heat flux along the entire capsule fore-body. The experimental data shows a localized increase in the heat flux measurement around a position of $z/R = -0.5$. This artifact has been attributed to real, non-laminar, or unsteady flow phenomenon occurring in the test section and has been observed in other experimental campaigns according to Hollis [35]. At the higher angles of attack of 20, 24, 28, and 32 degrees, good agreement is again shown for both the surface pressure and heat flux in comparison to the data by LAURA and the experimental measurements. The experimental data again sees a localized increase in heating at the 20-degree angle of attack, however, this artifact vanishes at the highest three angles. The CHAMPS NBS-Cart solver solution consistently remains within the estimated experimental uncertainty for all conditions.

At the highest angle of attack tested for the CEV vehicle, no heat flux measurement artifact is shown in the experimental data on the windward side. Without this phenomenon present, very good agreement is shown between all three data sets on the windward side. Overall, only minor disagreements in the final heat flux are shown between both sets of numerical data.

4.3. Case 3 - AS-202 capsule

Validation of the TCNE solver will be performed on the AS-202 reentry capsule [36]. Numerical data is available for comparison from the work of Wright et al. [19] using the DPLR code with a grid study at the $t = 4510$ s trajectory point. The same trajectory point is simulated here to test the NBS-Cart solvers ability to accurately capture the wake heating profile on the capsule aft-body. Results are also presented for the fore-body pressure and heating profiles which has been confirmed by a grid study on the current solver. The freestream conditions for this trajectory point are listed in Table 3. A freestream mixture composition of 76.7% N_2 and 23.3% O_2 is assumed in this work. To save on computational cost, the published DPLR solution [19] did not account for the side slip angle for the grid study and trajectory sweep with the exception of one case to demonstrate the impact of the mild side slip angle on the heating profile. Since comparison against the DPLR grid converged solution at $t = 4510$ s is sought, no side slip angle is modeled in this work either.

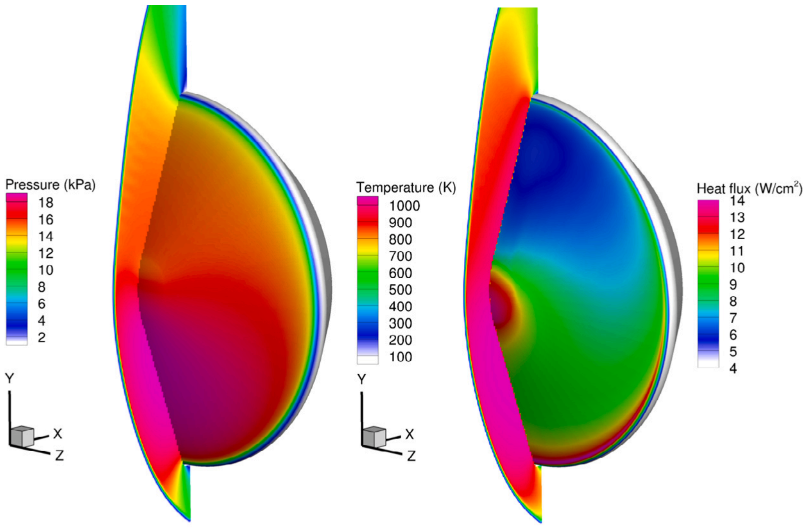

(a) Surface Pressure (b) Surface heat flux

Fig. 24. Surface pressure and heat flux profiles on the MSL capsule at Mach 9.47 and a 16-degree angle of attack.

Table 3
Freestream conditions for the AS-202 re-entry vehicle at the $t = 4510$ trajectory point.

Time (s)	Alt. (km)	Re_D	U_∞ (km/s)	M	ρ_∞	T_∞	α (deg)	β (deg)
4510	66.0	3.2×10^5	7.80	25.6	1.69×10^{-4}	230	17.8	2.5

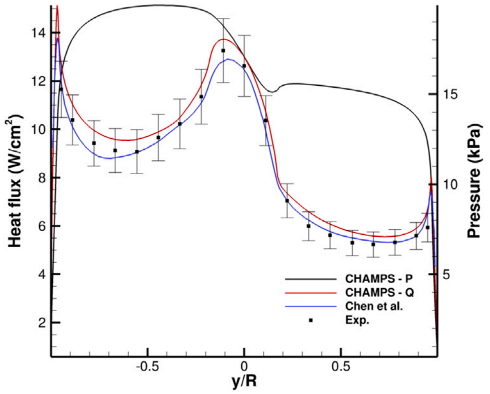

Fig. 25. Heat flux profile along XY plane for the MSL capsule at 16-degrees.

The surface boundary condition is a diffusion-limited, fully catalytic surface to N_2 and O_2 recombination with a radiative equilibrium temperature boundary condition. The wall is assumed to have an emissivity of 0.89 to align with DPLR [19].

Flow visualization of the temperature, vibrational temperature, N_2 mass fraction, and O_2 mass fraction around the capsule are shown in Fig. 30. Volume slices were extracted at the Y = 0 and Z = 0 planes with both temperature contours set to the same contour limits. Significant levels of thermal non-equilibrium is realized, especially as the flow expands around the capsule shoulder where the temperature rapidly cools down to around 2500 K while the vibrational temperature remains around 6000 K. In the expansion region, oxygen is almost completely dissociated and nitrogen has dissociated substantially as well resulting in a region dominated by atomic species and hence, raising the vibrational temperature relaxation time to give way to significant thermal non-equilibrium. In the subsonic recirculation zone behind the capsule, the lower flow velocity and higher concentration of molecular species results in temperatures closer to equilibrium.

Good shock and wake structure resolution is realized with the use of the CHAMPS Cartesian-AMR solver. The shock front is tracked only within a limited range in front of the capsule fore-body and is allowed to deresolve away beyond the shoulder extents. The peak temperature is predicted to be on the order of 13,000 K, however, due to the first order reduction at the shock front to remove unphysical artifacts, the true peak temperature is expected to be slightly higher. Ionization effects could be expected to occur given these post-shock conditions, however, they are not modeled in this work. A better look at the shock and wake tracking by the AMR is shown in Fig. 31. Shock tracking is performed on the finest grid level due to the close proximity of the shock front to the surface while wake tracking is performed on the second finest level to be consistent with the resolution used on the aft-body. This setup avoids having coarse-fine interfaces close to the surface within the wake flow region which could inhibit the final surface solution.

A grid study was performed on the NBS grid resolution to ensure adequate capturing of relevant surface quantities. Since the aft-body heating can be sensitive to the accurate modeling of the shear layer coming from the leeward shoulder and off the aft apex, the surface resolution (SR) is also allowed to vary in this grid study in combination with the wall-normal resolution and surface cell size. Fig. 32 shows the grid convergence study on the fore and aft-body heating and pressure profiles taken at the symmetry plane. Employing 75 wall-normal grid points on the NBS solver shows an under-resolved surface heating profile which quickly grid converges upon additional wall-normal resolution. In terms of the cell size at the surface, the heating profile is invariant for both the fore and aft-body profiles. Minor adjustments are shown upon increasing the surface resolution by about 30%, particularly in the aft-body wake region. Overall, good grid convergence is shown and no variations in surface pressure were observed for any grid model. Taking the second grid to be the reference solution for the NBS-Cart solver, 4.24 million grid points were used on the Cartesian solver while the NBS used approximately 11,000 surface elements with 100 wall-normal points for a total of 1.1 million elements. The total model size was then set at 5.3 million grid points.

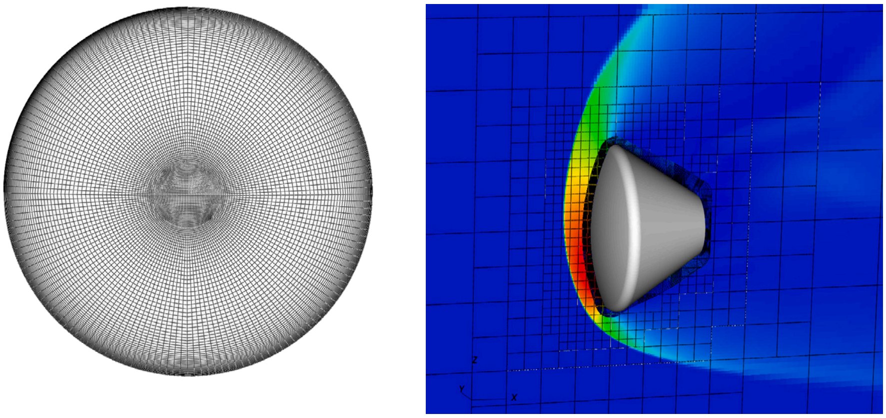

(a) Surface Grid (b) NBS-Cart

Fig. 26. NBS-Cart computational model schematic for the Orion CEV at a 16-degree angle of attack. The Orion CEV and surface grid is visualized as well as the NBS volume mesh and Cartesian block-structure.

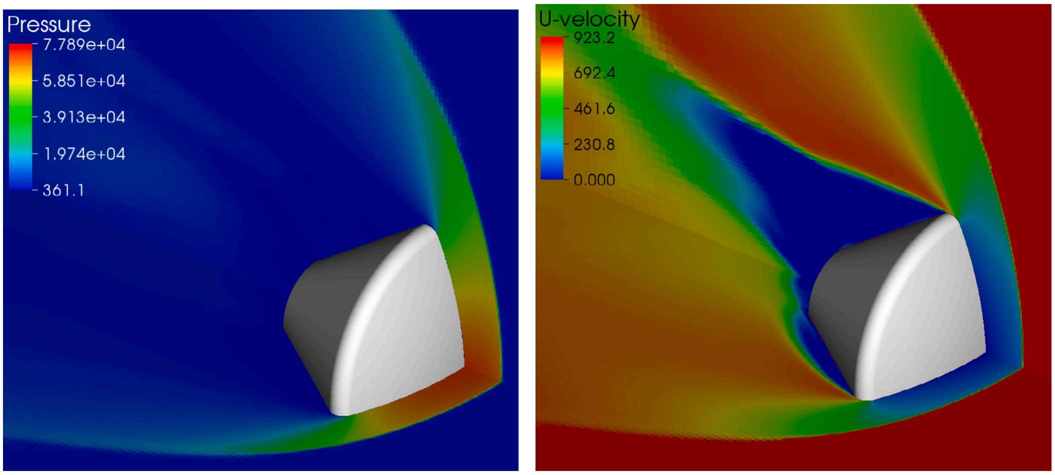

(a) Pressure (b) U-velocity

Fig. 27. Pressure and u-velocity contours around the Orion CEV at a 16-degree angle of attack.

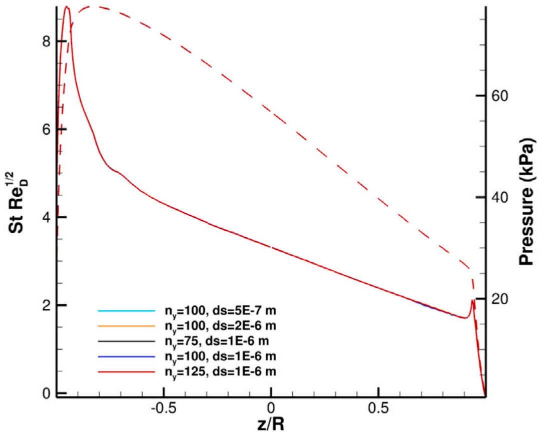

Fig. 28. Grid resolution study on the Orion CEV at a 32-degree angle of attack in terms of surface pressure and heat flux. Solid lines denote heat flux profiles while dashed lines denote pressure profiles.

The heat flux to the surface was broken down into its three contributions from the translational/rotational mode (Q_{tr}), vibrational component (Q_v), and enthalpy diffusion component (Q_{diff}). The vibrational energy flux contributes the least to the total heat flux (given in red) while the other energy modes contribute roughly equal contributions to the total heat load. The significant heating caused by surface catalysis highlights the importance of modeling the catalytic surface for these conditions. The wall temperature reaches a peak value of around 2200 K and closely follows the heat flux profile as expected. Looking at the aft-body heating, a comparison to the computed solution of Wright et al. [19] is provided showing generally good agreement on both the windward and leeward side of the vehicle (see Fig. 33). Some differences in the overall heating profile shape are shown in the wake region which has been attributed to differences in the numerical modeling employed by both codes. The DPLR grid was generated to maintain both shock and wake alignment for every trajectory point which may provide slightly improved capturing of the wake flow structure versus a non-aligned Cartesian grid. Furthermore, both sets of results employ a final grid structure that is close to fully grid converged, but some trade off is made for a reduced computational cost in exchange for reduced accuracy.

The AS-202 capsule aft body was also fitted with 23 calorimeters of which 19 were properly functioning during flight [36]. In Ref. [19], a best-fit line was computed based on the measured flight data (and excluding spurious measurements) and uncertainty bounds of ± 20%

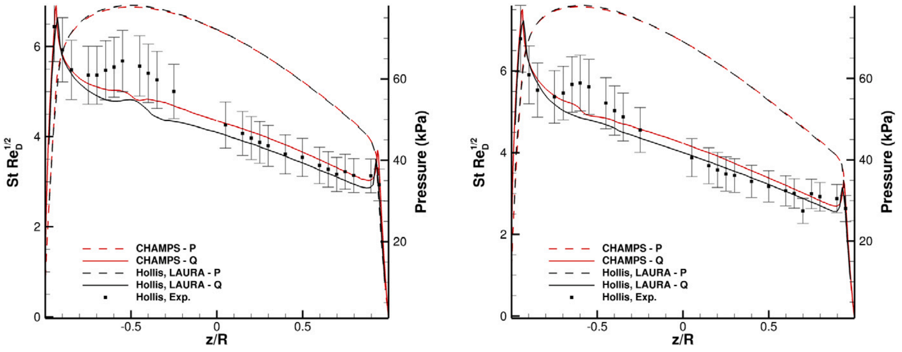

(a) 16-degree (b) 20-degree

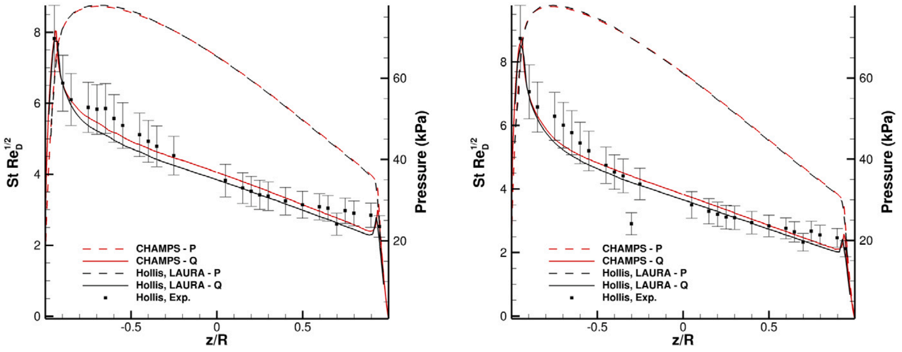

(c) 24-degree (d) 28-degree

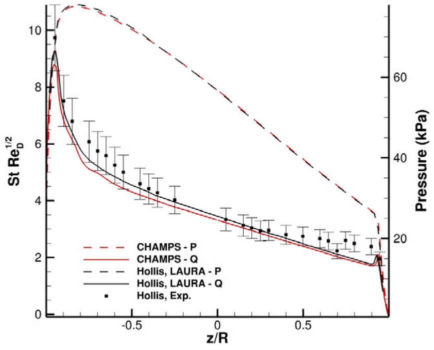

(e) 32-degree

Fig. 29. Computed data for surface pressure and surface heat flux for the Orion CEV at all angles of attack against LAURA and the experimental data.

were then applied to the best fit line [37]. Calorimeter locations have been labeled and schematically shown in Fig. 34. Full details of the calorimeter positions in the Cartesian reference frame (assuming the nose of the capsule to be at the origin) are given in Table 4 as well as the extracted lower and upper uncertainty bounds on each probe, the DPLR heat flux, and the CHAMPS NBS-Cart heat flux at each probe position. In general, the agreement with DPLR and with the flight data is good for most probe locations with some exceptions. The probes located in the attached flow region (probes a–d, f and g) see good alignment with the flight data with only probe f over-predicting the measured heating, similar to DPLR. It was shown in Ref. [19] that inclusion of the side-slip angle in the CFD simulation would improve the predicted heat flux prediction for calorimeter f. Flight data for this trajectory point of calorimeter i was not obtained and so comparison is made exclusively to DPLR. The largest disagreement in computed heat flux occurs for calorimeter s located just upstream of the capsule apex within the separated flow region. Similar low heating levels are predicted in this region by the current work and DPLR with the heat flux magnitude being similar to all other calorimeters in the wake region. The cause of this error is unknown and appears to not be linked to the side slip angle [19].

Taking the second NBS grid from the grid study as the reference, the surface skin friction and heating can be plotted on the aft-body to get a better look at the overall surface solution and the interaction of the wake structure on the surface (see Fig. 35). The skin friction coefficient clearly shows the initiation of the shear layer as the flow separates from the surface on the leeward side via a rapid drop-off in shear stress. The surface heating also drops off within the separated flow region with a localized peak heating point on the body apex. The general trends on the aft-body solution agree qualitatively well with the solution from DPLR.

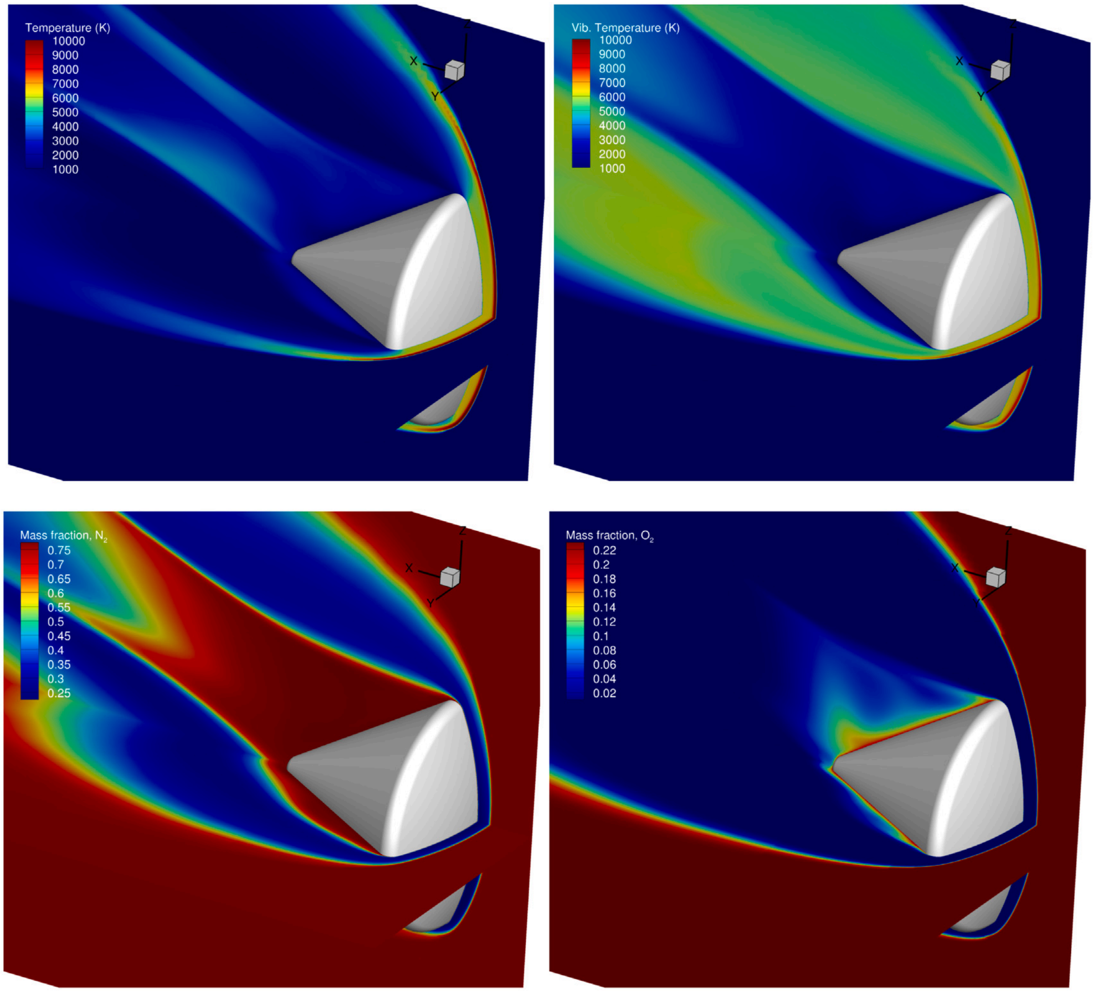

Fig. 30. Temperature and vibrational temperature flow-field around the AS-202 capsule at a 17.8-degree angle of attack (top) with N_2 and O_2 mass fractions show in the bottom row. Contours were extracted at the Y = 0 and Z = 0 planes.

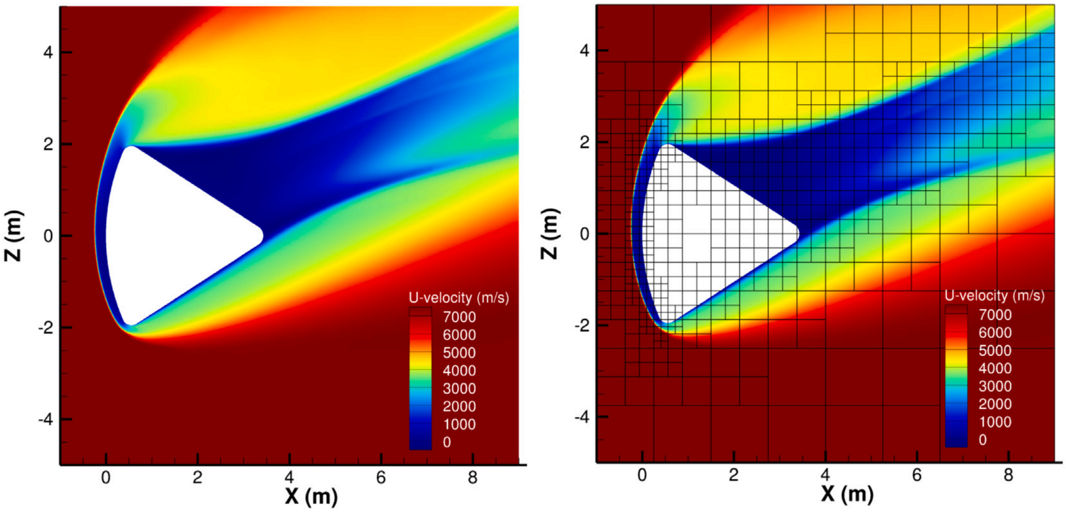

Fig. 31. U-velocity flow-field around the AS-202 capsule at a 17.8-degree angle of attack (left) with the Cartesian block-structure overlain (right). Shock tracking is performed on the finest level with wake tracking on the second finest level.

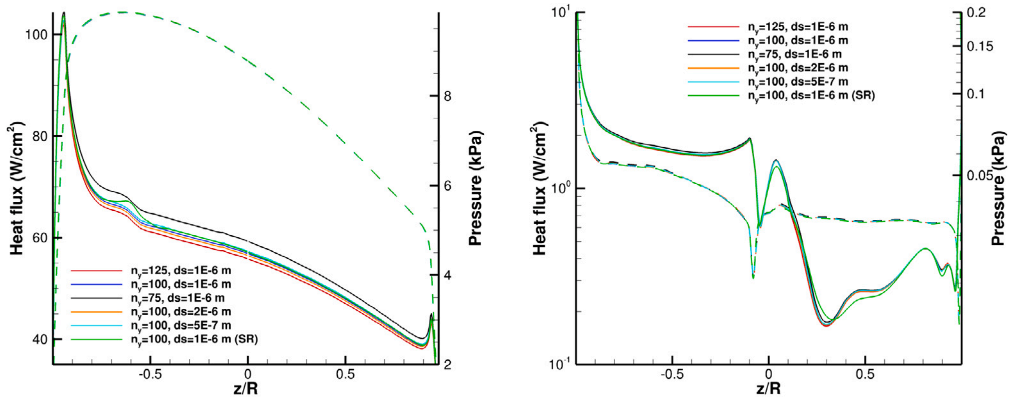

(a) fore-body (b) aft-body

Fig. 32. Line extracts of surface heat flux and wall pressure along the symmetry line for a grid convergence study on the NBS solver. “SR” represents an increase in surface resolution by 30%. Solid lines denote heat flux profiles while dashed lines denote pressure profiles.

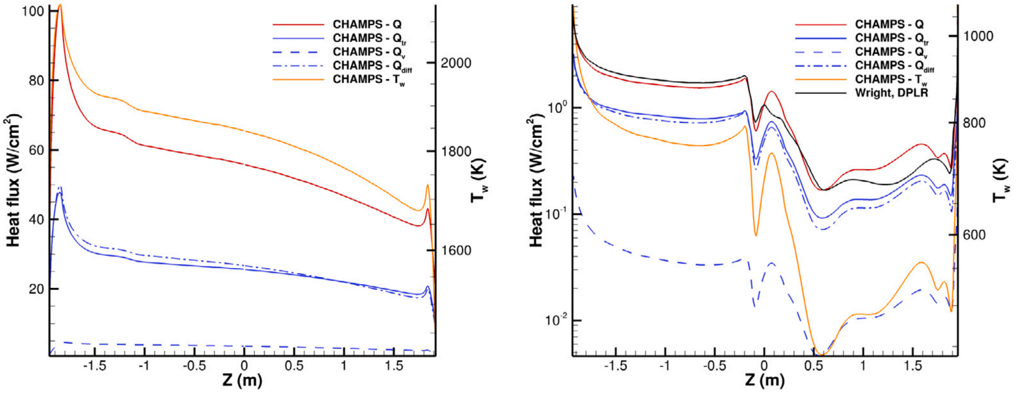

(a) fore-body (b) aft-body

Fig. 33. Line extracts of surface heat flux and wall temperature along the symmetry line for comparison against Wright et al. [19] with DPLR. The heat flux solution for CHAMPS is broken down into its individual contributions from different heating mechanisms.

Table 4
Aft body calorimeter positions in the Cartesian reference frame with comparison of measured in-flight heat flux uncertainty bounds to values predicted by DPLR and by the CHAMPS NBS-Cart solver.

Calorimeter				Flight Data		DPLR	CHAMPS
Name	X (m)	Y (m)	Z (m)	Lower bound	Upper bound		
a	1.2080	−0.1286	−1.5638	1.4792	2.2198	2.2000	2.0037
b	1.6980	0.0437	−1.2501	1.2965	1.9340	1.9184	1.7175
c	2.0560	0.4304	−0.9229	0.9961	1.5097	1.4086	1.4547
d	2.9480	−0.0505	−0.4362	1.1624	1.7360	1.7515	1.5865
e	3.4310	0.0000	0.0000	1.2630	1.8736	1.0164	1.1498
f	0.6950	1.4136	−1.2728	1.6757	2.5143	3.0922	2.8240
g	1.6150	1.0393	−0.7888	0.6495	0.9695	1.0315	0.9784
h	0.5450	1.9551	−0.0512	7.3712	10.995	9.9716	8.8399
i	0.5450	0.0000	1.9558	N/A	N/A	4.5981	4.0829
j	0.9410	1.7419	−0.0426	0.3340	0.5128	0.3481	0.2562
k	1.5760	1.3288	−0.0580	0.2630	0.3909	0.3870	0.4332
l	2.2880	0.8666	0.0439	0.3268	0.4898	0.3068	0.3378
m	1.0680	1.3548	0.9592	0.2938	0.4423	0.3209	0.2818
n	0.6950	1.3333	1.3567	0.6188	0.9277	0.6110	0.4849
o	1.3660	0.9465	1.1201	0.2561	0.3839	0.3200	0.3170
p	1.5260	0.8009	1.1023	0.3281	0.4893	0.2865	0.2794
q	1.8430	−0.1289	1.1495	0.2582	0.3932	0.2111	0.2539
r	2.0560	0.0391	1.0176	0.2375	0.3460	0.2078	0.2249
s	2.9480	0.0383	0.4374	1.2824	1.9327	0.2414	0.2430

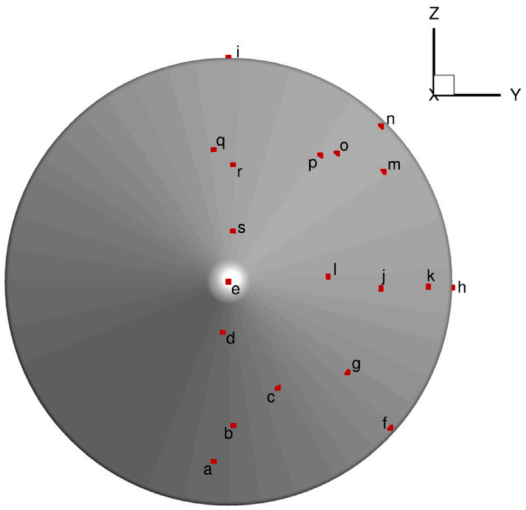

Fig. 34. AS-202 aft body calorimeter locations for all 19 functional probes.

The surface mass fractions for N_2 and O_2 are plotted on the fore and aft-body in Fig. 36. The recombination of N_2 appears to follow the opposite trend to O_2 recombination such that O_2 reaches close to its freestream mass fraction just aft of the leeward shoulder and appears to follow the separation line on the aft-body. Two localized peaks in surface heating are present on the leeward aft-body region resulting in increases in O_2 dissociation as denoted by a reduced mass fraction at the surface whereas N_2 sees fully recovery to its own freestream composition in this region. Looking at the fore-body profiles, minimal recombination is seen at the surface due to the higher surface temperature. These surface mass fraction contours highlight the level of chemical non-equilibrium both in the fore and aft body regions. The peak wall temperature on the windward shoulder is only slightly higher than 2000 K which is where oxygen begins to dissociate. A chemical equilibrium approximation would then result in oxygen fully recombining to its freestream composition on the surface which would increase the enthalpy diffusion flux and over-predict the total surface heating. An equilibrium composition would also significantly affect the level of thermal non-equilibrium in the system by enforcing more rapid recombination of all atomic species into their molecular counterparts resulting in lower vibrational relaxation times due to higher molecular species content.

5. Conclusion

The extension of the near-body Cartesian solver inside CHAMPS is outlined for simulating complex three-dimensional flow-fields of hypersonic vehicles at non-zero angles of attack. The solver was tested on a scale Mars Science Lander and the Orion Crew Exploration Vehicle showing good agreement for low enthalpy flows. The solver was then tested on the AS-202 capsule in a 5-species air mixture at a 17.8-degree angle of attack, demonstrating the efficient shock and wake tracking capabilities of the CHAMPS Cartesian solver while efficiently resolving the fore and aft body heating profiles in a more realistic high-enthalpy environment. The formulated solver has been shown to be very effective at capturing surface heating loads, which are known to be sensitive to the employed numerical method, while retaining a comparable computational cost to traditional body-fitted approaches in terms of total grid points. The use of the near-body Cartesian solver simplifies the time-to-solution process for a typical CFD workflow by removing the need for a manually generated volume grids in place of a simpler surface grid. Future work aims at targeting higher order, low-dissipation numerical schemes to be used in resolved transitional and turbulent flow structures as well as simulating more complex flight vehicles to further highlight the advantages of the solver.

Declaration of competing interest

The authors declare that they have no known competing financial interests or personal relationships that could have appeared to influence the work reported in this paper.

Data availability

Data will be made available on request.

Acknowledgments

The authors would like to recognize and show appreciation for the financial support provided by NASA Kentucky EPSCoR RA, USA Award no. 80NSSC19M0144 with E. Stern as the technical monitor, NASA EPSCoR R3, USA Award no. 80NSSC19M0084 with M. Barnhardt as the technical monitor, and from the NASA ACCESS program, USA award no. 80NSSC21K1117. The authors would also like to thank the collaborators from NASA Ames Research Center, NASA Langley Research Center, and the NASA Johnson Space Center. The funding support provided by the DoD HPC Modernization Program, USA under contract FA700-19-2-0002 with Dr. Russ Cummings (Director of Hypersonic Vehicle Simulation Institute (HVSI)) as program manager is also gratefully acknowledged.

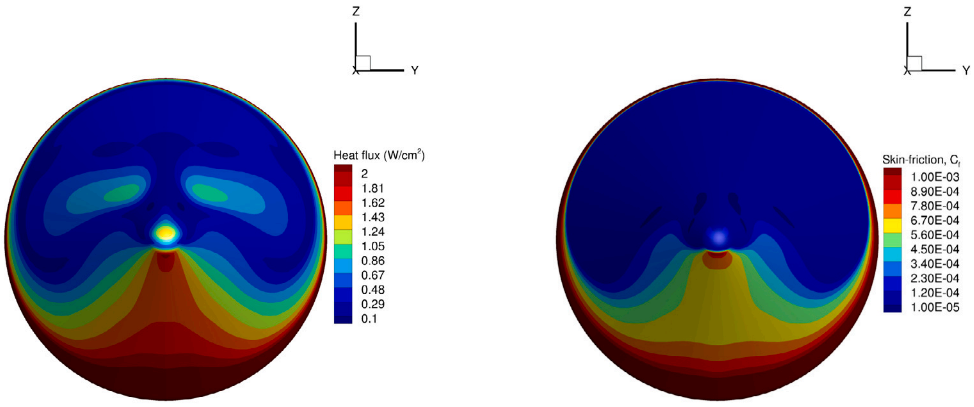

(a) Heat flux

(b) Skin-friction

Fig. 35. Surface heat flux (left) and skin-friction (right) on the AS-202 aft-body showing the wake structure interaction with the computed surface solution.

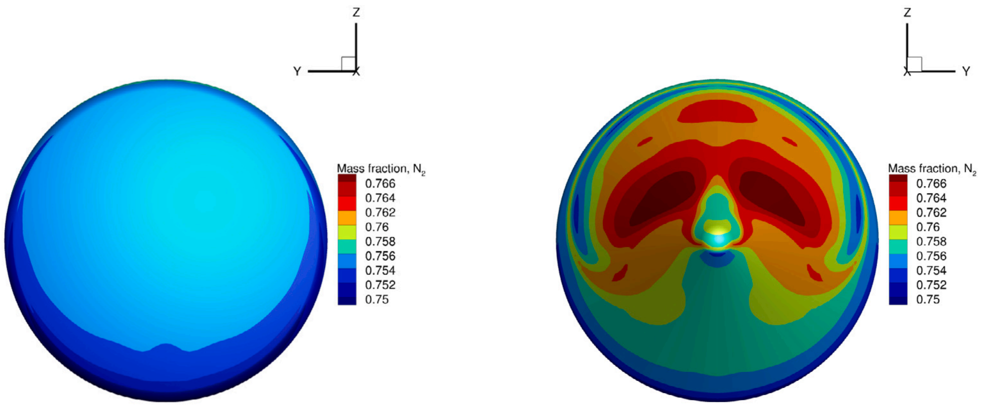

(a) fore-body, N_2 (b) aft-body, N_2

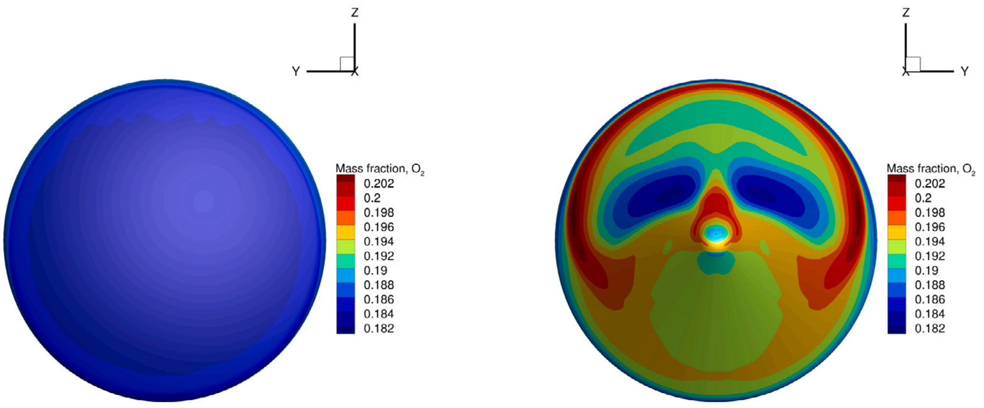

(c) fore-body, O_2 (d) aft-body, O_2

Fig. 36. Surface mass fractions showing N_2 (top) and O_2 (bottom) recombination on the fore (left) and aft (right) body of the AS-202 capsule.

Appendix A. Governing equations

The following section provides further details on the employed governing equations, the modeling of the transport properties, and the evaluation of the chemical source term for a fluid in thermo-chemical non-equilibrium. The total energy of a multi-component fluid is described by

$$E = \sum_{s}^{ns} \rho_s C v_{tr,s} T + \sum_{s}^{ns} \rho_s e_{v,s} + \sum_{s}^{ns} \rho_s h_s^o + \frac{1}{2}\rho(u^2 + v^2 + w^2). \tag{A.1}$$

The translational and rotational specific heats at constant volume are assumed to be constant and given by

$$C v_{t,s} = \frac{3}{2}\frac{R_u}{M_s} \tag{A.2}$$

and

$$C v_{r,s} = \begin{cases} \frac{R_u}{M_s} & \text{for molecules,} \\ 0 & \text{for atoms and electrons.} \end{cases} \tag{A.3}$$

where R_u is the universal gas constant and M_s is the molecular weight of species s. The total vibrational energy is then defined as

$$E_v = \sum_{s}^{ns} \rho_s e_{v,s} \tag{A.4}$$

with,

$$e_{v,s} = \begin{cases} \sum_{i=1}^{m} g_{s,i} \frac{R_u}{M_s} \frac{\theta_{v,s,i}}{\exp(\theta_{v,s,i}/T_{ve})-1} & \text{for molecules,} \\ 0 & \text{for atoms and electrons,} \end{cases} \tag{A.5}$$

where $\theta_{v,s,i}$ is the species characteristic vibrational temperature for species s and vibrational mode i, m denotes the number of vibrationally-activated energy modes for a given species, and $g_{s,i}$ denotes the degeneracy of the ith energy level of species s. Diatomic molecules can be modeled by a single vibrational energy level with a degeneracy of unity while polyatomic species may have several vibrational energy levels. The specific heat at constant volume for the vibrational mode may then be given by

$$\begin{aligned} C v_{v,s} &= \frac{\partial e_{v,s}}{\partial T_v} \\ &= \begin{cases} \sum_{i=1}^{m} g_{s,i} \frac{R_u}{M_s} \frac{(\theta_{v,s,i}/T_v)^2 \exp(\theta_{v,s,i}/T_v)}{(\exp(\theta_{v,s,i}/T_v)-1)^2} & \text{for molecules,} \\ 0 & \text{for atoms and electrons.} \end{cases} \end{aligned} \tag{A.6}$$

Appendix B outlines the various constants used for modeling the vibrational effects.

The mixture viscosity, thermal conductivity, and species diffusion coefficient is computed with the Gupta mixing rule [18]. The species viscosity can be calculated with

$$\mu = \sum_{s\neq e} \frac{m_s\gamma_s}{\sum_{r\neq e}\gamma_r\Delta^{(2)}_{sr}(T) + \gamma_e\Delta^{(2)}_{se}(T_v)} + \frac{m_e\gamma_e}{\sum_r \gamma_r\Delta^{(2)}_{er}(T_v)}, \tag{A.7}$$

where the molar concentration is defined as

$$\gamma_s = \frac{\rho_s}{\rho M_s} \tag{A.8}$$

and the molar concentration is

$$m_s = \frac{M_s}{N_a} \tag{A.9}$$

such that N_a is Avogadro's number. Then, the translational, rotational, and thermal conductivities may be defined as

$$\kappa_t = \frac{15}{4} k_{b,SI} \sum_{s\neq e} \frac{\gamma_s}{\sum_{r\neq e} a_{sr}\gamma_r\Delta^{(2)}_{sr}(T) + 3.54\gamma_e\Delta^{(2)}_{se}(T_v)}, \tag{A.10}$$

$$\kappa_r = k_{b,SI} \sum_{s=mol.} \frac{\gamma_s}{\sum_{r\neq e}\gamma_r\Delta^{(1)}_{sr}(T) + \gamma_e\Delta^{(1)}_{se}(T_v)}, \tag{A.11}$$

and

$$\kappa_v = k_{b,SI}\frac{Cv_v}{R_u} \sum_{s=mol.} \frac{\gamma_s}{\sum_{r\neq e}\gamma_r\Delta^{(1)}_{sr}(T) + \gamma_e\Delta^{(1)}_{se}(T_v)}. \tag{A.12}$$

The constant, a_{sr}, is defined as

$$a_{sr} = 1 + \frac{(1-(m_s/m_r))(0.45 - 2.54(m_s/m_r))}{(1+(m_s/m_r))^2}, \tag{A.13}$$

and $k_{b,SI}$ is the Boltzmann constant in SI units. The collision terms for computing the mixture properties are defined as

$$\Delta^{(1)}_{sr}(T) = \frac{8}{3}\sqrt{\frac{2M_sM_r}{\pi R_u T(M_s+M_r)}}\,10^{-20}\pi\Omega^{(1,1)}_{sr}(T) \tag{A.14}$$

and

$$\Delta^{(2)}_{sr}(T) = \frac{16}{5}\sqrt{\frac{2M_sM_r}{\pi R_u T(M_s+M_r)}}\,10^{-20}\pi\Omega^{(2,2)}_{sr}(T). \tag{A.15}$$

The collision integrals $\pi\Omega^{(1,1)}_{sr}$ and $\pi\Omega^{(2,2)}_{sr}$ were taken from the work of Wright et al. [38].

The mass diffusion flux is assumed to follow Fick's first law as shown in Eq. (A.16) where $\nabla \boldsymbol{Y}_s$ is the gradient of the species mass fraction and D_s is the species diffusion coefficient. The mass diffusion flux is given as

$$\boldsymbol{I}_s = -\rho D \nabla \boldsymbol{Y}_s. \tag{A.16}$$

Sutton and Gnoffo (1998) [39] have noted that Fick's law does not guarantee that the mass diffusion fluxes will sum to zero resulting in errors in capturing the correct mass fraction gradients among other errors. Modified Fick's law is used in this work to improve the solution accuracy and is given by

$$\boldsymbol{J}_{s\neq e} = \boldsymbol{I}_s - Y_s\sum_{r\neq e}^{ns}\boldsymbol{I}_r, \tag{A.17}$$

where e denotes the electron species (not included in this work) since the charge neutrality of the flow-field must be handled separately. The species binary diffusion coefficient for heavy particle collisions is computed as

$$D_{sr} = \frac{k_{b,SI}T}{p\Delta^{(1)}_{sr}(T)}. \tag{A.18}$$

The species diffusion coefficient to be used in the governing equations that accounts for all interactions is then given by

$$D_s = \frac{\gamma_t^2 M_s(1-M_s\gamma_s)}{\sum_{r\neq s}\gamma_r/D_{sr}}, \tag{A.19}$$

with

$$y_t = \sum_s \gamma_s. \tag{A.20}$$

The viscous shear stresses are modeled based on a Newtonian fluid using Stokes' hypothesis

$$\tau_{ij} = \mu\left(\frac{\partial u_j}{\partial x_i} + \frac{\partial u_i}{\partial x_j}\right) + \lambda\frac{\partial u_k}{\partial x_k}\delta_{ij}, \tag{A.21}$$

where,

$$\lambda = -\frac{2}{3}\mu, \tag{A.22}$$

and the heat fluxes are accounted for using Fourier's law as

$$\boldsymbol{q_{tr}} = -\kappa_{tr}\nabla\boldsymbol{T} \tag{A.23}$$

and

$$\boldsymbol{q_v} = -\kappa_v\nabla\boldsymbol{T_v}. \tag{A.24}$$

Finally, looking in more detail at the formulation of the chemical source term, the forward reaction rate is computed using an Arrhenius curve fit for the Park two-temperature model using the empirical coefficients given in Appendix C as,

$$k_{fr} = A_{fr}T_c^{\eta_r}\exp\left(-\frac{T_{ar}}{T_c}\right), \tag{A.25}$$

where,

$$T_c = T^{a_f}T_{ve}^{b_f}. \tag{A.26}$$

Here, A_{fr} and η_r are coefficients for the Arrhenius curve fit, T_c is the forward controlling temperature, and T_{ar} represents the activation temperature. The values used for the Arrhenius curve fit can be found in Table C.1. The backward controlling reaction rate is a function of the forward reaction rate and the equilibrium constant, K_c, as computed using the backward controlling temperature, T_{bc},

$$k_{br}(T_{bc}) = \frac{k_{fr}(T_{bc})}{K_c(T_{bc})}, \tag{A.27}$$

where the backward controlling temperature is defined in Eq. (A.28) as

$$T_{bc} = T^{a_b}T_{ve}^{b_b}. \tag{A.28}$$

For all dissociation reactions, the forward controlling temperature is computed using $a_f = 0.5$ and $b_f = 0.5$ whereas the backward dissociation reactions are computed using $a_b = 1$ and $b_b = 0$. For exchange reactions, $a_f = a_b = 1$ and $b_f = b_b = 0$. The equilibrium constant is computed using a NASA 9 polynomial curve fit for the normalized entropy and enthalpy of each species which may then be used to compute the normalized Gibb's free energy for each species [40]. The Gibb's free energy is defined as

$$\hat{g}_s = \hat{h}_s - T_{bc}\hat{s}_s, \tag{A.29}$$

where $\hat{g}_s$ is the Gibbs energy per unit mole for species s, $\hat{h}_s$ is the enthalpy per unit mole of species s, and $\hat{s}_s$ is the entropy per unit mole for species s. The curve fits for the species enthalpy and entropy are given by

$$\frac{\hat{h}_s}{R_uT_{bc}} = -a_{1s}\frac{1}{T_{bc}^2} + a_{2s}\frac{\ln(T_{bc})}{T_{bc}} + a_{3s} + a_{4s}\frac{T_{bc}}{2} + a_{5s}\frac{T_{bc}^2}{3} + a_{6s}\frac{T_{bc}^3}{4} + a_{7s}\frac{T_{bc}^4}{5} + a_{9s}\frac{1}{T_{bc}} \tag{A.30}$$

and

$$\frac{\hat{s}_s}{R_u} = -a_{1s}\frac{1}{2T_{bc}^2} - a_{2s}\frac{1}{T_{bc}} + a_{3s}\ln(T_{bc}) + a_{4s}T_{bc} + a_{5s}\frac{T_{bc}^2}{2} + a_{6s}\frac{T_{bc}^3}{3} + a_{7s}\frac{T_{bc}^4}{4} + a_{10s}. \tag{A.31}$$

The equilibrium constant is a function of the change in the Gibbs free energy between the reactants and products and is given by

$$K_c = \exp\left[-\sum_{s=1}^{ns}\left((\upsilon''_{sr} - \upsilon'_{sr})\frac{\hat{g}_s}{R_uT_{bc}}\right)\right]\left(\frac{p_0}{R_uT_{bc}}\right)^{\upsilon_r}. \tag{A.32}$$

The value of p_0 is a reference pressure set to 1 bar, while in the computational framework, p_0 is set to 0.1 and R_u is set to 8.31441 to be in the CGS unit system. The coefficients for the enthalpy and entropy curve fits are taken from the work of Gordon and McBride [41].

The translational-vibrational energy exchange source term, S_{t2v}, is based on the Landau–Teller formulation [42] given by

$$S_{t2v} = \sum_{s=mol.} \rho_s \frac{e_{v,s}(T) - e_{v,s}(T_v)}{\tau_s}, \tag{A.33}$$

where $e_{v,s}(T)$ is the species vibrational energy at equilibrium which is computed using the translational-rotational temperature, $e_{v,s}(T_v)$ is the species vibrational energy computed using the vibrational temperature, and τ_s is the relaxation time with the summation being taken over the molecular species only. The relaxation time is defined based on the molar averaged Landau–Teller relaxation time, $\langle \tau_s \rangle$ as

$$\tau_s = \langle \tau_s \rangle + \tau_{ps}, \tag{A.34}$$

and τ_{ps} is Park's correction on the relaxation time for high-temperature effects beyond 8000 K [20]. The molar averaged relaxation time can be found with Eq. (A.35)

$$\langle \tau_s \rangle = \frac{\sum_r X_r}{\sum_r X_r / \tau_{sr}}, \tag{A.35}$$

where τ_{sr} is the inter-species Landau–Teller relaxation time which is modeled using a semi-empirical relation by Millikan and White for temperatures between 300 K and 8000 K as [43]

$$\tau_{sr} = \frac{p_0}{p} \exp\left[A_{sr} \left(T^{-1/3} - B_{sr} \right) - 18.42 \right]. \tag{A.36}$$

The coefficients A_{sr} and B_{sr} are functions of the reduced molecular weight, μ_{sr}, and $\theta_{v,s}$ and defined as

$$A_{sr} = 0.0016 \mu_{sr}^{1/2} \theta_{v,s}^{4/3} \tag{A.37}$$

and

$$B_{sr} = 0.015 \mu_{sr}^{1/4} \tag{A.38}$$

where,

$$\mu_{sr} = \frac{M_s M_r}{M_s + M_r}. \tag{A.39}$$

The characteristic vibrational temperature, $\theta_{v,s}$, used in the vibrational relaxation model corresponds to the first vibrationally activated energy level as it is assumed that the relaxation rate is dominated by the fastest energy level. The Park relaxation time correction is then defined based on the effective collision cross-section, σ_s, the average molecular velocity of species s, c_s, and the number density of the species, N_s, as

$$\tau_{ps} = \frac{1}{\sigma_s c_s N_s}, \tag{A.40}$$

where,

$$\sigma_s = \sigma_s' \left(\frac{50000}{T} \right)^2 \quad \text{in m}^2 \tag{A.41}$$

and

$$c_s = \sqrt{\frac{8 R_u T}{\pi M_s}}. \tag{A.42}$$

In Eq. (A.41), σ_s' is an empirical factor used to correlate the numerical approximation to the experimental data [44]. Hence, this parameter would generally be species dependent, however, in this work, σ_s' is held fixed at a value of 10^{-20}. The energy exchange into the vibrational energy mode due to chemical reactions is computed using the non-preferential model as

$$S_{c2v} = \sum_{s=mol.} \omega_s e_{v,s}. \tag{A.43}$$

Table B.1
Basic species molecular and viscosity data.

Species	M_s (g/mol)	h_s^o (J/kg)	g_m	θ_v (K)
N_2	28	0.0000000E0	1	3395.0
O_2	32	0.0000000E0	1	2239.0
NO	30	2.9961230E6	1	2817.0
N	14	3.3621610E7	1	0.0
O	16	1.5431190E7	1	0.0

Appendix B. Species energy state and transport property data

Table B.1 outlines the various species used in this work with their respective molecular weights, enthalpy of formation at 0 K (taken from Mutation++ [45]), and vibrational energy data.

Appendix C. Arrhenius curve fit coefficients

Table C.1 outlines all the dissociation and exchange reactions included within this work as well as the relevant parameters required to compute the forward reaction rates. The rates used here were taken from the work of Park et al. [46] with the rates from reaction 4 taken from Bose and Candler [47].

Appendix D. Eigenvector matrices for perfect gas Steger–Warming flux

The right eigenvector matrix R for a non-reacting, single species mixture is given as

$$\begin{bmatrix} \frac{1}{a^2} & 0 & 0 & \frac{1}{2a^2} & \frac{1}{2a^2} \\ \frac{u}{a^2} & t_x & m_x & \frac{1}{2a^2}\left(u + a n_x\right) & \frac{1}{2a^2}\left(u - a n_x\right) \\ \frac{v}{a^2} & t_y & m_y & \frac{1}{2a^2}\left(v + a n_y\right) & \frac{1}{2a^2}\left(v - a n_y\right) \\ \frac{w}{a^2} & t_z & m_z & \frac{1}{2a^2}\left(w + a n_z\right) & \frac{1}{2a^2}\left(w - a n_z\right) \\ \frac{\alpha}{a^2} & \hat{v} & \hat{w} & \frac{1}{2a^2}(H + a\hat{u}) & \frac{1}{2a^2}(H - a\hat{u}) \end{bmatrix}, \tag{D.1}$$

where the face normal vector is defined as $\boldsymbol{n} = \{n_x, n_y, n_z\}$, the face tangential vectors as $\boldsymbol{t} = \{t_x, t_y, t_z\}$ and $\boldsymbol{m} = \{m_x, m_y, m_z\}$, H is the total enthalpy, $\hat{v}$ is the contravariant velocity associated with $\boldsymbol{t}$, and $\hat{w}$ is the contravariant velocity associated with $\boldsymbol{m}$. The parameter α and the total enthalpy is defined as

$$\alpha = \frac{1}{2} \boldsymbol{V} \cdot \boldsymbol{V} \tag{D.2}$$

and

$$H = \frac{a^2}{\gamma - 1} + \alpha. \tag{D.3}$$

The left eigenvector is then taken as the inverse of R and is given as (see Eq. (D.4) in Box I) where γ is the specific heat ratio for air set to 1.4.

Appendix E. Eigenvector matrices for TCNE Steger–Warming flux

The right eigenvector matrix R for a multi-component gas mixture is given as

$$\begin{bmatrix} \frac{\delta_{sr}}{a^2} & \cdots & 0 & 0 & \frac{Y_s}{2a^2} & \frac{Y_s}{2a^2} & 0 \\ \vdots & \ddots & \vdots & \vdots & \vdots & \vdots & \vdots \\ \frac{u}{a^2} & \cdots & l_x & m_x & \frac{u+an_x}{2a^2} & \frac{u-an_x}{2a^2} & 0 \\ \frac{v}{a^2} & \cdots & l_y & m_y & \frac{v+an_y}{2a^2} & \frac{v-an_y}{2a^2} & 0 \\ \frac{w}{a^2} & \cdots & l_z & m_z & \frac{w+an_z}{2a^2} & \frac{w-an_z}{2a^2} & 0 \\ \frac{2\beta\alpha-\tilde{\gamma}_r}{\beta a^2} & \cdots & \hat{v} & \hat{w} & \frac{H+a\hat{u}}{2a^2} & \frac{H-a\hat{u}}{2a^2} & -\frac{\phi}{\beta a^2} \\ 0 & \cdots & 0 & 0 & \frac{e_v}{2a^2} & \frac{e_v}{2a^2} & \frac{1}{a^2} \end{bmatrix}, \tag{E.1}$$

Table C.1
Arrhenius curve fit coefficients for dissociation reactions.

	Reaction	Partner	T_c	A_{fr} (cm^3/mol · s)	η_r	T_{ar} (K)
1	$N_2 + M \rightleftharpoons N + N + M$	Molecules	$\sqrt{TT_v}$	7.00E21	−1.60	1.132E5
		Atoms	$\sqrt{TT_v}$	3.00E22	−1.60	1.132E5
2	$O_2 + M \rightleftharpoons O + O + M$	Molecules	$\sqrt{TT_v}$	2.00E21	−1.50	5.936E4
		Atoms	$\sqrt{TT_v}$	1.00E22	−1.50	5.936E4
3	$NO + M \rightleftharpoons N + O + M$	Other	$\sqrt{TT_v}$	5.00E15	0.00	7.550E4
		NO, N, O	$\sqrt{TT_v}$	1.10E17	0.00	7.550E4
4	$O_2 + N \rightleftharpoons NO + O$		T	2.49E9	1.18	4.010E3
5	$N_2 + O \rightleftharpoons NO + N$		T	6.00E13	0.10	3.8000E4

$$\begin{bmatrix} a^2-\alpha\,(\gamma-1) & (\gamma-1)\,u & (\gamma-1)\,v & (\gamma-1)\,w & -(\gamma-1) \\ -\hat{v} & t_x & t_y & t_z & 0 \\ -\hat{w} & m_x & m_y & m_z & 0 \\ \alpha\,(\gamma-1)-\hat{u}a & an_x-(\gamma-1)\,u & an_y-(\gamma-1)\,v & an_z-(\gamma-1)\,w & (\gamma-1) \\ \alpha\,(\gamma-1)+\hat{u}a & -an_x-(\gamma-1)\,u & -an_y-(\gamma-1)\,v & -an_z-(\gamma-1)\,w & (\gamma-1) \end{bmatrix}, \tag{D.4}$$

Box I.

$$\begin{bmatrix} a^2\delta_{sr}-Y_s\tilde{\gamma}_r & \cdots & \beta uY_s & \beta vY_s & \beta wY_s & -\beta Y_s & -\phi Y_s \\ \vdots & \ddots & \vdots & \vdots & \vdots & \vdots & \vdots \\ -\hat{v} & \cdots & l_x & l_y & l_z & 0 & 0 \\ -\hat{w} & \cdots & m_x & m_y & m_z & 0 & 0 \\ \tilde{\gamma}_r-\hat{u}a & \cdots & an_x-\beta u & an_y-\beta v & an_z-\beta w & \beta & \phi \\ \tilde{\gamma}_r+\hat{u}a & \cdots & -an_x-\beta u & -an_y-\beta v & -an_z-\beta w & \beta & \phi \\ -e_v\tilde{\gamma}_r & \cdots & \beta ue_v & \beta ve_v & \beta we_v & -\beta e_v & a^2-\phi e_v \end{bmatrix}. \tag{E.7}$$

Box II.

where δ_{sr} is the kronecker delta and s denotes a species row in the matrix while r denotes a species column and the total enthalpy (per unit mass for the TCNE solver) of a multi-component mixture is defined as

$$H = \sum_{s=1}^{ns} Y_s e_s + \alpha + \frac{p}{\rho}, \tag{E.2}$$

and e_s is the internal energy of species s given by

$$e_s = Cv_{tr,s}T + e_{v,s} + h_s^o. \tag{E.3}$$

From Ref. [48], β and ϕ are defined as the partial derivative of the mixture pressure with respect to the total and vibrational energy respectively while $\tilde{\gamma}_r$ is defined as the partial derivative of the mixture pressure with respect to the species densities. The equations are then given as

$$\beta = \frac{\partial p}{\partial E} = \frac{R_u}{\rho Cv_{tr}} \sum_{s=1}^{ns} \frac{\rho_s}{M_s}, \tag{E.4}$$

$$\phi = \frac{\partial p}{\partial E_v} = -\beta, \tag{E.5}$$

and

$$\tilde{\gamma}_r = \frac{\partial p}{\partial \rho_r} = \frac{R_u T}{M_r} + \beta\alpha - \beta e_r - \phi e_{v,r}. \tag{E.6}$$

Eqs. (E.4)–(E.6) are simplified versus Ref. [48] due to the lack of any ionization modeling in this work. Then, the left eigenvector matrix may be defined as (see Eq. (E.7) in Box II).

References

[1] Slotnick J, Khodadoust A, Alonso J, Darmofal D, Gropp W, Lurie E, et al. CFD vision 2030 study: A path to revolutionary computational aerosciences. Tech. Rep. NASA/CR-2014-218178, Hampton, Virginia: National Aeronautics and Space Administration; 2014.

[2] Meakin RL, Wissink AM, Chan WM, Pandya SA, Sitaraman J. On strand grids for complex flows. In: 18th AIAA computational fluid dynamics conference. AIAA paper 2007-3834, Miami, Florida; 2007, p. 1–18. http://dx.doi.org/10.2514/6.2007-3834.

[3] Brahmachary S, Natarajan G, Kulkarni V, Sahoo N. A sharp-interface immersed boundary method for high-speed compressible flows. In: Immersed boundary method: Design and applications. Springer; 2020, p. 251–75. http://dx.doi.org/10.1007/978-981-15-3940-4_9.

[4] Sekhar SK, Ruffin SM. Predictions of convective heat transfer using a cartesian grid solver for hypersonic flows. In: Fluid dynamics and co-located conferences. 44th AIAA thermophysics conference, San Diego, CA: AIAA; 2013, p. 1–17. http://dx.doi.org/10.2514/6.2013-2645.

[5] Arslanbekov R, Kolobov V, Frolova A. Analysis of compressible viscous flow solvers with adaptive cartesian mesh. In: 20th AIAA computational fluid dynamics conference. Honolulu, Hawaii: AIAA; 2011, http://dx.doi.org/10.2514/6.2011-3381.

[6] Baskaya AO, Capriati MC, Ninni D, Bonelli F, Pascazio G, Turchi A, et al. Verification and validation of immersed boundary solvers for hypersonic flows with gas-surface interactions. In: AIAA aviation forum. American Institute of Aeronautics and Astronautics; 2022, http://dx.doi.org/10.2514/6.2022-3276.

[7] Wissink AM, Katz AJ, Chan WM, Meakin RL. Validation of the strand grid approach. In: 19th AIAA computational fluid dynamics conference. AIAA paper 2009-3792, San Antonio, Texas; 2020, p. 1–21. http://dx.doi.org/10.2514/6.2009-3792.

[8] Wissink AM, Sitaraman J, Katz AJ, Roget B. Application of 3D strand mesh technology to rotorcraft hover. In: 53rd AIAA aerospace sciences meeting. Kissimmee, Florida; 2015, p. 1–19.

[9] Jain R, Biedron RT, Jones WT, Lee-Rausch EM. Modularization and validation of FUN3D as a CREATE™-AV helios near-body solver. In: AIAA science and technology forum and exposition 2016. American Institute of Aeronautics and Astronautics; 2016, http://dx.doi.org/10.2514/6.2016-1298.

[10] Aref P, Ghoreyshi M, Jirasek A, Seidel J. Application of the HPCMP CREATE™-AV kestrel to an integrated propeller prediction. Aerospace 2020;7:1–19. http://dx.doi.org/10.3390/aerospace7120177.

[11] McQuaid JA, Zibitsker AL, Martin A, Brehm C. Heat flux predictions for high speed flows with an immersed boundary method. In: AIAA aviation forum. American Institute of Aeronautics and Astronautics; 2021, http://dx.doi.org/10.2514/6.2021-3145.

[12] Zibitsker AL, McQuaid JA, Brehm C, Martin A. Fully coupled simulation of low temperature ablator and hypersonic flow solver. In: AIAA science and technology forum and exposition 2022. American Institute of Aeronautics and Astronautics; 2022, http://dx.doi.org/10.2514/6.2021-0926.

[13] Zibitsker AL, McQuaid JA, Brehm C, Martin A. Study of a two-dimensional shape change of blunt-body geometries at hypersonic conditions using fully-coupled simulation. In: AIAA aviation forum. American Institute of Aeronautics and Astronautics; 2022, http://dx.doi.org/10.2514/6.2022-4006.

[14] McQuaid JA, Zibitsker AL, Martin A, Brehm C. Simulation of graphite ablation using an overset near body solver on an adaptive block-structured cartesian off-body grid. In: AIAA aviation forum. American Institute of Aeronautics and Astronautics; 2022, http://dx.doi.org/10.2514/6.2022-4088.

[15] Zibitsker AL, McQuaid JA, Brehm C, Martin A. Study of graphite ablation at arc-jet conditions using finite-rate and equilibrium chemistry models. In: Eleventh international conference on computational fluid dynamics. 2022.

[16] Zibitsker AL, McQuaid JA, Brehm C, Martin A. Validation and analysis of a coupled fluid-ablation framework for modeling low-temperature ablator. Int J Heat Mass Transfer 2024;218. http://dx.doi.org/10.1016/j.ijheatmasstransfer.2023.124728.

[17] Park C. Assessment of two-temperature kinetic model for ionizing air. J Thermophys Heat Transfer 1989;3:233–44. http://dx.doi.org/10.2514/3.28771.

[18] Gupta RN, Yos JM, Thompson RA, Lee K-P. A review of reaction rates and thermodynamic and transport properties for an 11-species air model for chemical and thermal nonequilibrium calculations to 30,000 K. Tech. Rep. NASA-RP-1232, National Aeronautics and Space Administration; 1990.

[19] Wright MJ, Prabhu DK, Martinez ER. Analysis of the apollo command module afterbody heating part I: AS-202. J Thermophys Heat Transfer 2006;20:16–30. http://dx.doi.org/10.2514/1.15873.

[20] Park C. Nonequilibrium hypersonic aerothermodynamics. 1st ed.. Moffet Field, California: Wiley-Interscience; 1990.

[21] Higgins JC, Browne OM, Brehm C. Adaptive mesh refinement for a sharp immersed boundary method. In: AIAA scitech forum. American Institute of Aeronautics and Astronautics; 2021, http://dx.doi.org/10.2514/6.2021-0747.

[22] Secco NR, Kenway GKW, He P, Mader C, Martins JRRA. Efficient mesh generation and deformation for aerodynamic shape optimization. AIAA J 2021;59:1151–68. http://dx.doi.org/10.2514/1.J059491.

[23] Karypis G, Kumar V. A fast and high quality multilevel scheme for partitioning irregular graphs. SIAM J Sci Comput 1999;20:359–92. http://dx.doi.org/10.1137/S1064827595287997.

[24] Browne OMF, Haas AP, Fasel HF, Brehm C. An efficient linear wavepacket tracking method for hypersonic boundary-layer stability prediction. J Comput Phys 2018;380:243–68. http://dx.doi.org/10.1016/j.jcp.2018.11.028.

[25] Jiang G-S, Shu C-W. Efficient implementation of weighted ENO schemes. J Comput Phys 1996;126:202–28. http://dx.doi.org/10.1006/jcph.1996.0130.

[26] Liu X-D, Osher S, Chan T. Weighted essentially non-oscillatory schemes. J Comput Phys 1994;115:200–12. http://dx.doi.org/10.1006/jcph.1994.1187.

[27] Brehm C, Barad MF, Housman JA, Kiris CC. A comparison of higher-order finite-difference shock capturing schemes. Comput & Fluids 2015;122:184–208. http://dx.doi.org/10.1016/j.compfluid.2015.08.023.

[28] Ducros F, Ferrand V, Nicoud F, Weber C, Darracq D, Gacherieu C, et al. Large-Eddy simulation of the shock/turbulence interaction. J Comput Phys 1999;152:517–49. http://dx.doi.org/10.1006/jcph.1999.6238.

[29] Nishikawa H. A truncation error analysis of third-order MUSCL scheme for nonlinear conservation laws. Internat J Numer Methods Fluids 2020;93:1031–52. http://dx.doi.org/10.1002/fld.4918.

[30] Steger JL, Warming RF. Flux vector splitting for the inviscid gasdynamic equations with applications to finite difference methods. J Comput Phys 1981;40:263–93. http://dx.doi.org/10.1016/0021-9991(81)90210-2.

[31] Wright MJ, Candler GV, Bose D. Data-parallel line relaxation method for the Navier–Stokes equations. AIAA J 1998;36:1603–9. http://dx.doi.org/10.2514/2.586.

[32] Hollis BR, Collier AS. Turbulent aeroheating testing of Mars science laboratory entry vehicle. J Spacecr Rockets 2008;45:417–27. http://dx.doi.org/10.2514/1.31798.

[33] Chen S-s, Yan C, Zhong K, Xue H-c, Li E-l. A novel flux splitting scheme with robustness and low dissipation for hypersonic heating prediction. Int J Heat Mass Transfer 2018;127:126–37.

[34] Shu C-w, Osher S. Efficient implementation of essentially non-oscillatory shock-capturing schemes. J Comput Phys 1988;77:439–71.

[35] Hollis BR. Experimental investigation of project orion crew exploration vehicle aeroheating: LaRC 20-inch mach 6 air tunnel test 6931. Tech. Rep. NASA/TM-2009-215718, Hampton, Virginia: National Aeronautics and Space Administration; 2009.

[36] Lee DB, Bertin JJ, Goodrich WD. Heat-transfer rate and pressure measurements obtained during apollo orbital entries. Tech. Rep. NASA TN D-6028, Manned Spacecraft Center; 1970.

[37] Murthy AV, Tsai BK, Saunders RD. Radiative calibration of heat-flux sensors at NIST: Facilities and techniques. J Res Natl Inst Stand Technol 2000;105:229–300. http://dx.doi.org/10.6028/jres.105.033.

[38] Wright MJ, Bose D, Palmer GE, Levin E. Recommended collision integrals for transport property computations, part 1: Air species.. AIAA J 2005;43:2558–64. http://dx.doi.org/10.2514/1.16713.

[39] Sutton K, Gnoffo PA. Multi-component diffusion with application to computational aerothermodynamics. In: 7th AIAA/ASME joint thermophysics and heat transfer conference. AIAA; 1998, http://dx.doi.org/10.2514/6.1998-2575.

[40] Gordon S, McBride BJ. Computer program for calculation of complex chemical equilibrium compositions and applications, Part I: Analysis. Tech. Rep. NASA-RP-1311, NASA Lewis Research Center; 1994.

[41] McBride BJ, Heimel S, Ehlers JG, Gordon S. Thermodynamic properties to 6000K for 210 substances involving the first 18 elements. Tech. Rep. NASA-SP-3001, NASA Lewis Research Center; 1963.

[42] Vincenti WG, Kruger CH. Equilibrium gas properties. In: Introduction to physical gas dynamics. 1st ed.. Krieger Publishing Company; 1975, p. 152–96.

[43] Millikan RC, White DR. Systematics of vibrational relaxation. J Chem Phys 1963;39:3209–13. http://dx.doi.org/10.1063/1.1734182.

[44] Park C, Howe JT, Jaffe RL. Review of chemical-kinetic problems of future NASA missions, II: Mars entries. J Thermophys Heat Transfer 1994;8:9–23. http://dx.doi.org/10.2514/3.496.

[45] Scoggins JB, Leroy V, Bellas-Chatzigeorgis G, Dias B, Magin TE. Mutation++: Multicomponent thermodynamic and transport properties for ionized gases in C++. SoftwareX 2020;12. http://dx.doi.org/10.1016/j.softx.2020.100575.

[46] Park C, Jaffe RL, Partridge H. Chemical-kinetic parameters of hyperbolic Earth entry. J Thermophys Heat Transfer 2001;15:76–90. http://dx.doi.org/10.2514/2.6582.

[47] Bose D, Candler GV. Thermal rate constants of the $O_2 + N \rightarrow NO + O$ reaction based on the A2' and A4' potential-energy surfaces. J Chem Phys 1997;107:6136–45. http://dx.doi.org/10.1063/1.475132.

[48] Gnoffo PA, Gupta RN, Shinn JL. Conservation equations and physical models for hypersonic air flows in thermal and chemical nonequilibrium. Tech. Rep. NASA-RP-2867, National Aeronautics and Space Administration; 1989.